

A grounded perspective on New Early Dark Energy using ACT, SPT, and BICEP/Keck

Juan S. Cruz^a Florian Niedermann^b Martin S. Sloth^a

^aCP3-Origins, Center for Cosmology and Particle Physics Phenomenology, University of Southern Denmark, Campusvej 55, 5230 Odense M, Denmark

^bNordita, KTH Royal Institute of Technology and Stockholm University Hannes Alfvéns väg 12, SE-106 91 Stockholm, Sweden

E-mail: jcr@sdu.dk, florian.niedermann@su.se, sloth@cp3.sdu.dk

Abstract. We examine further the ability of the New Early Dark Energy model (NEDE) to resolve the current tension between the Cosmic Microwave Background (CMB) and local measurements of H_0 and the consequences for inflation. We perform new Bayesian analyses, including the current datasets from the ground-based CMB telescopes Atacama Cosmology Telescope (ACT), the South Pole Telescope (SPT), and the BICEP/Keck telescopes, employing an updated likelihood for the local measurements coming from the SH_0ES collaboration. Using the SH_0ES prior on H_0 , the combined analysis with Baryonic Acoustic Oscillations (BAO), Pantheon, Planck and ACT improves the best-fit by $\Delta\chi^2 = -15.9$ with respect to Λ CDM, favors a non-zero fractional contribution of NEDE, $f_{\text{NEDE}} > 0$, by 4.8σ , and gives a best-fit value for the Hubble constant of $H_0 = 72.09$ km/s/Mpc (mean 71.49 ± 0.82 with 68% C.L.). A similar analysis using SPT instead of ACT yields consistent results with a $\Delta\chi^2 = -23.1$ over Λ CDM, a preference for non-zero f_{NEDE} of 4.7σ and a best-fit value of $H_0 = 71.77$ km/s/Mpc (mean 71.43 ± 0.85 with 68% C.L.). We also provide the constraints on the inflation parameters r and n_s coming from NEDE, including the BICEP/Keck 2018 data, and show that the allowed upper value on the tensor-scalar ratio is consistent with the Λ CDM bound, but, as also originally found, with a more blue scalar spectrum implying that the simplest curvaton model is now favored over the Starobinsky inflation model.

Keywords: cosmological parameters from CMBR, cosmological phase transitions, cosmology of theories beyond the SM, dark energy theory

Contents

1	Introduction	1
2	The NEDE model	3
3	Data analysis and results	7
3.1	MCMC Analysis	7
3.2	Study of NEDE including ACT	8
3.2.1	Establishing the Baseline Model	9
3.2.2	Results and Discussion	9
3.3	Study of NEDE including SPT	13
3.4	Consequences for Inflation using BICEP	15
4	Discussion and summary	17
A	Complementary results for MCMC analyses of the different runs	19
B	Individual chi2 for the different chains presented	22

“Keep your eyes on the stars, but your feet on the ground.”
—Theodore Roosevelt

1 Introduction

The current standard model of cosmology is the Λ CDM model. It portrays the contents of the Universe as perfect fluids, with the different components observing particular equations of state. These are specifically: a cosmological constant, cold dark matter, baryonic matter, and radiation. The model is the result of combining general relativity and the cosmological principle, i.e. the assumption that the Universe is homogeneous and isotropic, and specifying the energy-momentum tensor as a sum of the aforementioned components. The first two give out the FLRW type metric, which features a scale factor and allows the Hubble parameter to be defined. However, only after all these ingredients are included does one have a complete cosmological model.

Λ CDM is simple enough as to be described by six free parameters (assuming no spatial curvature): $\{\omega_b, \omega_c, \theta_*, \tau_{\text{reio}}, A_s, n_s\}$, where the last two are related to the inflationary era. Since its introduction, it has been extremely successful at explaining the Universe we observe, but a new generation of measurements is putting it to the test [1, 2]. Different current experiments show growing tensions in some of the parameters derived from Λ CDM. The largest tension so far is that of the Hubble parameter at present time, H_0 [3, 4].

The tension arises from the disagreement between values inferred from the CMB at high redshifts, most notoriously $H_0 = 67.27 \pm 0.60$ km/s/Mpc from the Planck collaboration [5], and those from local measurements at lower redshifts, which are mostly obtained, but not only, by constructing a distance ladder using standard candles. The SH_0ES collaboration [6] stands out among them, reporting a value of 73.04 ± 1.04 km/s/Mpc. There are many more measurements on both categories still in line with the trend of an early- versus late-time discrepancy, however, with larger errors. It is worth mentioning that at low values of redshift, the dependence of these measurements on the Λ CDM model is only mild, while the CMB measurement, although extremely precise, relies heavily on the model to evolve the fitted parameters to its present values. These two measurements claim high enough

precision for their mean values to present us with the so-called *Hubble tension* at around 5σ or more, depending on the datasets combined. Local under densities and other systematics have already been considered, and so far, it is not possible to explain the tension as being a consequence of only systematic issues [7–10]

Assuming the reported tension is not simply due to unknown systematic errors, a modification of the underlying model and assumptions must be considered. Several models have been put out in an attempt to explain the tension (see [11] for a review), but few models truly reduce the tension over Λ CDM when all the data, including CMB, BAO, and SN data, are included. The most promising models have been compared with each other under reasonable criteria and ranked according to how well they reduce the Hubble tension in the cosmological data [12]. Future data will be able to better constrain and discriminate between the few top phenomenologically favored models. Thus, further improvement of the models and testing them against more data is currently an important task.

The Hubble tension is closely related to the sound horizon [3, 13–15]. As with H_0 , the size of the sound horizon at recombination, r_s^{rec} , or alternatively at the baryon drag epoch, r_s^{d1} , is different when deduced from CMB measurements and when it is obtained from the classical distance ladder (CDL) together with BAO. The latter, when combined with Supernovae (SNe) data, fixes the product $H_0 r_s$ without assuming the Λ CDM model. This seems to point at solutions to the tension that change the cosmic evolution just prior to recombination.

Along with the Hubble tension, an additional tension in the cosmological parameter σ_8 has been observed. As explained in further detail in the reviews and papers [2, 16–18], there is a tension between 2σ and 3σ among low and high redshift measurements for the strength of matter clustering given by $S8 \equiv \sigma_8 \sqrt{\Omega_m/0.3}$. The parameter σ_8 measures the amplitude of the power spectrum at the scale of $8h^{-1}$ Mpc and is known to lie roughly between 0.7 and 1.0. Early time measurements seem to prefer higher values of σ_8 [19–22] while local measurements favor smaller values for it [5]. A generic feature of [New] Early Dark Energy ([N]EDE) type models is the slight increase in the baryonic and cold dark matter which has been seen to raise the value of σ_8 with a small statistically insignificant amount over Λ CDM [23–29].

In this article we concentrate on one of the models proposed to address the Hubble tension by reducing the size of the sound horizon at recombination/last-scattering, the New Early Dark Energy (NEDE) model [25, 30]. It has been successful in reducing the tension when compared against data from Planck, BAO, SN Pantheon, and SH_0ES while increasing slightly the σ_8 tension in its first simple implementation, also later referred to as Cold NEDE. A newer proposal², the Hot NEDE model [33, 34] may lead to different conclusions and holds in it the potential to reduce the σ_8 tension as well, however, we do not consider Hot NEDE in the present study. In [12, 25], Cold NEDE has also been compared to its predecessor EDE [23, 35–37], and it has been previously tested against CMB ground base data from the Atacama Cosmology Telescope [38]. Similarly, data from SPT and ACT has already been used to constrain the EDE model [38–42]. The objective of this paper is to update the statistics of the Cold NEDE model by including more datasets in the analysis. Although our main focus is to make an update in relation to the more relevant Hubble tension, we also report on the favored σ_8 values. Specifically, we are performing the corresponding Bayesian analysis with data coming from ACT, SPT, and BICEP together with our baseline datasets consisting of BAO, SNe, and Planck data. Our approach is slightly different from previous studies [38] in which the multi-modality of NEDE is examined by separating the mass range. We instead perform our analysis under the assumption of a fixed equation of state and arrive at similar conclusions.

In the original work, it was already shown that NEDE prefers a much bluer spectrum of

¹They appear to differ by a few percent in a relatively model-independent way.

²For other interesting developments of NEDE, see also [31, 32].

the initial adiabatic primordial curvature perturbation from inflation, which has important consequences for our understanding of inflation [25, 30]. However, here, using BICEP/keck 2018 data, we provide for the first time a full $n_s - r$ constraints plot for NEDE (although a parametric estimate of it was given earlier in [43]). It looks qualitatively similar to the findings made within old EDE [23, 35, 37] and shows that a simple curvaton model [44–46] is now favored over the Starobinsky inflation model [47].

The present paper is organized as follows. In section 2 we summarize the model and establish the terminology and notation relevant for the rest of the document. In the next one, section 3, we describe the details of the Monte Carlo Markov Chain (MCMC) analysis, and discuss our results. It is subdivided into three sections, one for each new dataset: ACT, SPT, and BICEP. In the last section, we gather the most relevant observations and comment on the prospects of the NEDE model.

2 The NEDE model

We start by introducing a phenomenological NEDE model as a general formalism for describing a phase transition in the CMB that can capture the physics of different field theoretic implementations such as cold, hot, and hybrid NEDE. Its distinctive feature is a *trigger mechanism* that induces a sudden decay of an early dark energy component ρ_{NEDE} at (cosmological) time $t = t_*(\mathbf{x})$ (which in general is a function of the spatial coordinate \mathbf{x}). The NEDE fluid at the background level is then described in terms of a time-dependent equation of state parameter

$$w_{\text{NEDE}}(t) = \begin{cases} -1 & \text{for } t < \bar{t}_* \\ w_{\text{NEDE}}(t) & \text{for } t \geq \bar{t}_* \end{cases}, \quad (2.1)$$

where \bar{t}_* arises from decomposing $t_*(\mathbf{x}) = \bar{t}_* + \delta t_*(\mathbf{x})$ into a background and fluctuation part.

Before the transition ρ_{NEDE} behaves like a cosmological constant, i.e. $\rho_{\text{NEDE}}(t < \bar{t}_*) = \bar{\rho}_{\text{NEDE}}^* = \text{const}$. In particular, it leads to an energy injection in the cosmic fluid that lowers the sound horizon r_s . Since the CMB measures the angular scale of r_s with high precision, the reduction in r_s needs to be compensated by shortening the distance to the last scattering surface, which is achieved by raising H_0 . Provided the fraction of NEDE, $f_{\text{NEDE}} = \rho_{\text{NEDE}}^*/\rho_{\text{tot}}^*$, is of order of 10% and the transition happens around matter-radiation equality, the increase in H_0 is large enough to reconcile the CMB-inferred value of H_0 with the locally measured one.

After the transition, $w_{\text{NEDE}}(t)$ is allowed to have a complicated time-dependence within the bounds $1/3 \leq w_{\text{NEDE}}(t \geq \bar{t}_*) \leq 1$, corresponding to a decay of ρ_{NEDE} at least as fast as radiation as expected in the bubble coalescence phase after the transition [25, 30] (see also [48]). This quick decay of NEDE is crucial to preserving the fit to the CMB power spectrum and having a viable late-time phenomenology. To be specific, after decomposing $\rho_{\text{NEDE}} = \bar{\rho}_{\text{NEDE}}(t) + \delta\rho_{\text{NEDE}}(t, \mathbf{x})$, we have

$$\bar{\rho}_{\text{NEDE}}(t) = \bar{\rho}_{\text{NEDE}}^* \exp\left\{-3 \int_{\bar{t}_*}^t d\tilde{t} H [1 + w_{\text{NEDE}}(\tilde{t})]\right\}, \quad (2.2)$$

where $H = \dot{a}/a$ is the Hubble parameter and we solved the energy conservation equation, $\dot{\bar{\rho}}_{\text{NEDE}} + 3H(1 + w_{\text{NEDE}})\bar{\rho}_{\text{NEDE}} = 0$, subject to the boundary condition $\bar{\rho}_{\text{NEDE}}(\bar{t}_*) = \bar{\rho}_{\text{NEDE}}^*$. Here and henceforth an asterisk denotes evaluation at decay time t_* .

Within this general description, we can capture the presence of the trigger in terms of a function $q(t, \mathbf{x})$. It defines the transition time $t_*(\mathbf{x})$ through the implicit condition

$$q(t_*(\mathbf{x}), \mathbf{x}) = q_* = \text{const}. \quad (2.3)$$

For example, in cold and hybrid NEDE, which relies on a scalar field trigger ϕ , we set $q = \phi$ and identify q_* with the threshold value ϕ_* at which quantum tunneling becomes efficient or

the field rolls over the watershed-like saddle, respectively. On the other hand, in Hot NEDE, we use the dark sector temperature T_d as a trigger and accordingly set $q = T_d$.

The trigger mechanism has important implications for the perturbations within the NEDE fluid. Before the transition, we have $\delta\rho_{\text{NEDE}} = 0$ because a cosmological constant does not support its own adiabatic perturbations (due to the constancy of $\bar{\rho}_{\text{NEDE}}$). After the transition, however, $\bar{\rho}_{\text{NEDE}}$ is a quickly decaying fluid, which will support its own fluctuations $\delta\rho_{\text{NEDE}} \neq 0$. They are seeded at the transition time t_* by the perturbations of the trigger, $\delta q_*(\mathbf{x}) \equiv \delta q(\bar{t}_*, \mathbf{x})$, where we decomposed

$$q(t, \mathbf{x}) = \bar{q}(t) + \delta q(t, \mathbf{x}). \quad (2.4)$$

These perturbations constitute dark sector acoustic oscillations and are a crucial part of the NEDE phenomenology. In particular, they lead to an excess decay of the Weyl potential, which balances the gravitational effect of an increased dark matter energy density (see the discussions in [25, 49, 50]). They also make NEDE phenomenologically distinct from other early dark energy models.

The precise relation between δq_* and $\delta\rho_{\text{NEDE}}^* \equiv \delta\rho_{\text{NEDE}}(\bar{t}_*)$ was derived in [25] by performing a fully covariant matching of the cosmological perturbation theory across the spacelike transition surface defined through Eq. 2.3. Here, we will provide an equivalent but slightly more intuitive derivation of the same relation. A spatial variation of Eq. 2.3 yields

$$\left(\frac{\partial q_*}{\partial t_*} \frac{\partial t_*}{\partial \mathbf{x}} + \frac{\partial q_*}{\partial \mathbf{x}} \right) \cdot d\mathbf{x} = 0, \quad (2.5)$$

which after substituting Eq. (2.4) becomes

$$\delta t_*(\mathbf{x}) = -\frac{\delta q_*(\mathbf{x})}{\dot{\bar{q}}_*}, \quad (2.6)$$

at linear order in δq , thus relating the trigger variations $\delta q_*(\mathbf{x})$, with variations of the transition time $\delta t_*(\mathbf{x})$. This formula can be understood intuitively as follows; when the trigger's value increases, i.e. $\dot{\bar{q}} > 0$, then for a positive perturbation $\delta q(\mathbf{x})$ the threshold value $q = q_*$ will be reached slightly earlier, which indeed translates to a negative $\delta t_*(\mathbf{x})$.

Now, the perturbations in ρ_{NEDE} arise because, due to the spatial dependence in Eq. 2.6, the fluid starts to decay at slightly different times at different positions in space. This can be described more formally by generalizing Eq. 2.2 to

$$\rho_{\text{NEDE}}(t, \mathbf{x}) \simeq \bar{\rho}_{\text{NEDE}}^* \exp \left\{ -3 \int_{t_*(\mathbf{x})}^t d\tilde{t} H [1 + w_{\text{NEDE}}(\tilde{t})] \right\}, \quad (2.7)$$

which is an expression for the full $\rho_{\text{NEDE}}(t, \mathbf{x})$, including perturbations, valid close to the transition, i.e. for $t \rightarrow t_*(\mathbf{x})$. The derivation of Eq. 2.7 is simple: We can always choose coordinates for which the transition surface is perfectly flat and hence $\delta q_* = 0$ (or $\delta t_* = 0$ equivalently). In this gauge $\delta\rho_{\text{NEDE}}(\bar{t}_*) = 0$ and thus the background formula in Eq. 2.2 is an arbitrarily good approximation for the full ρ_{NEDE} if evaluated sufficiently close to the transition surface (perturbations $\delta\rho_{\text{NEDE}}$ will be generated eventually due to gravitational sourcing). Transforming back to the original coordinates then yields Eq. 2.7, where the spatial dependence of $\rho_{\text{NEDE}}(t, \mathbf{x})$ arises from $t_*(\mathbf{x})$ in the lower integration limit. Finally, perturbing Eq. 2.7 and evaluating it at $t = t_*$ yields

$$\frac{\delta\rho_{\text{NEDE}}^*}{\bar{\rho}_*} = -3 [1 + w_{\text{NEDE}}(t_*)] H_* \frac{\delta q_*}{\dot{\bar{q}}_*}, \quad (2.8a)$$

where we used Eq. 2.6 to substitute for δt_* . This indeed agrees with the result obtained in [25]. There, a more exhaustive matching analysis also determines the initial velocity

divergence θ_{NEDE} , defined in momentum space through the perturbed energy momentum tensor as $ik^i(\delta T_{\text{NEDE}})_i^0 \equiv (1+w_{\text{NEDE}})\bar{\rho}_{\text{NEDE}} a \theta_{\text{NEDE}}$ alongside $\delta\rho_{\text{NEDE}} \equiv -(\delta T_{\text{NEDE}})_0^0$; explicitly,

$$\theta_{\text{NEDE}}^* = \frac{k^2 \delta q_*}{a_* \dot{q}_*}. \quad (2.8b)$$

In synchronous gauge the metric takes the form

$$ds^2 = -dt^2 + a(t)^2 (\delta_{ij} + h_{ij}) dx^i dx^j, \quad (2.9a)$$

where

$$h_{ij} = \frac{k_i k_j}{k^2} h + \left(\frac{k_i k_j}{k^2} - \frac{1}{3} \delta_{ij} \right) 6\eta, \quad (2.9b)$$

and $h = \delta^{ij} h_{ij}$. The evolution of $\delta_{\text{NEDE}} = \delta\rho_{\text{NEDE}}/\bar{\rho}_{\text{NEDE}}$ and θ_{NEDE} is then controlled by the two perturbation equations [51] (using cosmological time and neglecting spatial curvature)

$$\begin{aligned} \dot{\delta}_{\text{NEDE}} = & -3 [c_s^2 - w_{\text{NEDE}}(t)] H \delta_{\text{NEDE}} - [1 + w_{\text{NEDE}}(t)] \left(\frac{\theta_{\text{NEDE}}}{a} + \frac{\dot{h}}{2} \right) \\ & - 9 [1 + w_{\text{NEDE}}(t)] [c_s^2 - c_a^2] H^2 \frac{\theta_{\text{NEDE}}}{a} \frac{a^2}{k^2}, \end{aligned} \quad (2.10a)$$

$$\dot{\theta}_{\text{NEDE}} = - (1 - 3c_s^2) H \theta_{\text{NEDE}} + c_s^2 \frac{k^2}{a} \frac{\delta_{\text{NEDE}}}{1 + w_{\text{NEDE}}(t)}, \quad (2.10b)$$

where c_s is the effective sound speed in the fluid's rest-frame and the adiabatic sound speed is fixed in terms of w_{NEDE} ,

$$c_a^2 = w_{\text{NEDE}}(t) - \frac{1}{3} \frac{\dot{w}_{\text{NEDE}}(t)}{1 + w_{\text{NEDE}}(t)} \frac{1}{H}. \quad (2.11)$$

For simplicity, we assumed vanishing shear stress, $\sigma_{\text{NEDE}} = 0$, which is a fully self-consistent choice. The generalized equations in the presence of σ_{NEDE} and a phenomenological discussion thereof can be found in [25].

The system up this point provides a very general phenomenological framework applicable to different microscopic implementations. From here on, we will focus on Cold NEDE, discussed in detail in [25]. In this case, the trigger $q(t, \mathbf{x})$ is identified with a subdominant scalar field $\phi(t, \mathbf{x}) = \bar{\phi}(t) + \delta\phi(t, \mathbf{x})$. Before the transition it satisfies the background equation

$$\ddot{\bar{\phi}} + 3H\dot{\bar{\phi}} + m^2\bar{\phi} = 0. \quad (2.12)$$

In particular, it is frozen for $H \gg m$ due to the Hubble friction term. Once $H \lesssim m$, the field drops out of slow roll and starts to oscillate. For a radiation dominated universe, the solution is $\bar{\phi}(t) = \sqrt{2}\Gamma(5/4)\bar{\phi}_{\text{ini}}(H/m)^{1/4} J_{1/4}(\frac{m}{2H})$, where $J_{1/4}$ and Γ are the Bessel function of the first kind and the Gamma function, respectively. In particular, $\bar{\phi}/\bar{\phi}_{\text{ini}} \rightarrow 0$ as $H/m \rightarrow 0.18$. Cold NEDE uses the idea that ϕ triggers a first order phase transition in another field ψ as it approaches zero for the first time. This is achieved through the zero-temperature potential (assuming canonically normalized fields ψ and ϕ)

$$V(\psi, \phi) = \frac{\lambda}{4}\psi^4 + \frac{1}{2}M^2\psi^2 - \frac{1}{3}\alpha M\psi^3 + \frac{1}{2}m^2\phi^2 + \frac{1}{2}\tilde{\lambda}\phi^2\psi^2, \quad (2.13)$$

where α and λ are positive and dimensionless coefficients of order unity.³ This potential comes with two mass scales: the heavy scale $M \sim \text{eV}$ is setting the scale of NEDE and

³A similar model has been considered before in an inflationary context [52–54].

the ultralight scale $m \sim 10^{-27}\text{eV}$ makes sure that the trigger field starts to roll around matter-radiation equality. We further require $\alpha^2 > 4\lambda$ to ensure the right vacuum structure. Radiative stability of the trigger sector further demands $\tilde{\lambda} < \mathcal{O}(1) \times 10^3 m^2/M^2 \ll 1$. Initially the system sits at $(\psi, \phi) = (0, \phi_{\text{ini}})$ and is prevented from tunneling to its true minimum located at $(\psi, \phi)_{\text{t.v.}} = \left(\frac{M}{2\lambda}[\alpha + \sqrt{\alpha^2 - 4\lambda}], 0\right)$ by a huge potential barrier arising from the last term in Eq. 2.13. This barrier is eventually removed as ϕ starts to evolve towards smaller values. Tunneling becomes efficient when ϕ reaches a threshold value $\phi_* \ll \phi_{\text{ini}}$ corresponding to⁴ $H/m \approx 0.2$ (recall that the first zero crossing occurs as $H/m \rightarrow 0.18$, which corresponds to the removal of the last term in Eq. 2.13 and hence maximal tunneling probability). Within this model, we define NEDE as the energy that is released in the phase transition,

$$\bar{\rho}_{\text{NEDE}}^* = V(0, \phi_*) - V(\psi^{\text{t.v.}}, 0). \quad (2.14)$$

Having this type of triggered first-order phase transition achieves different things:

- The phase transition happens late enough in the expansion history to have an impact on the sound horizon r_s (without the trigger bubble percolation would happen much earlier when $H \sim \text{eV}$ without any noticeable effect on r_s).
- The transition is completed on very short time scales (compared to $1/H$). This avoids that bubbles grow too large, which would lead to additional (and potentially threatening) anisotropies in the CMB. Moreover, it makes sure that we can describe the colliding bubble wall condensate as a homogenous and isotropic fluid on large scales, corresponding to an evolution as in Eq. 2.7. It similarly justifies neglecting shear stress perturbations, $\sigma_{\text{NEDE}} = 0$, on these scales.
- The trigger field ϕ carries adiabatic fluctuations that seed acoustic oscillations in the decaying NEDE fluid, which, as we pointed out before, are a vital part of the NEDE phenomenology.

After the phase transition we are left with a large number of vacuum bubbles that expand and quickly start to collide with each other. On small scales, this field condensate is dominated by anisotropic stress. A crucial assumption then is that this manifests itself on large scale as an excess pressure that leads to a decay quicker than radiation, i.e. $w_{\text{NEDE}}(t > t_*) > 1/3$. Eventually, the condensate is expected to be converted into scalar field radiation and gravitational waves, corresponding to $w_{\text{NEDE}} \rightarrow 1/3$ (depending on the implementation other decay channels are possible too). As cosmological observables are only sensitive to ρ_{NEDE} when it is most dominant around the phase transition, we will approximate it as a constant, i.e. $w_{\text{NEDE}}(t > t_*) \approx w_{\text{NEDE}}^* = \text{const.}$

Cold NEDE has been implemented in the Boltzmann code **TriggerCLASS** [25]⁵, which builds on the Cosmic Linear Anisotropic Solving System **CLASS** [55]. It evolves the trigger field $\bar{\phi}$ with Eq. 2.12 alongside its adiabatic perturbations $\delta\phi$, governed by

$$\delta\ddot{\phi} + 2H\delta\dot{\phi} + (k^2/a^2 + m^2)\delta\phi = -\frac{1}{2}\dot{h}\dot{\phi}. \quad (2.15)$$

The matching Eqs. 2.8 at $t = t_*$ are then used to initialize the perturbations in the decaying NEDE fluid (δ_{NEDE} and θ_{NEDE}). Their subsequent evolution is described in terms of the system of Eqs. 2.10. The base model relies on the following choices: $(w_{\text{NEDE}}^*, c_s^2, H_*/m) = (2/3, 2/3, 0.2)$. Generalizations thereof are considered in [25]. The remaining model parameters are (i) the fraction of NEDE f_{NEDE} and (ii) the mass of the trigger field m . The latter

⁴Note that in the Cold NEDE model H/m is not a free parameter but theoretically predicted to be $H/m \approx 0.2$. In [30] we checked this prediction by treating it as a free parameter and found, as an experimental vindication of the trigger mechanism, that indeed the value $H/m \approx 0.2$ is also preferred by the data.

⁵<https://github.com/flo1984/TriggerCLASS>

determines the redshift z_* of the phase transition (or t_* equivalently) and can be inferred from the numerical background evolution. An approximation is given by

$$z_* \approx 2 \times 10^4 (1 - f_{\text{NEDE}})^{1/4} \left(\frac{3.4}{g_{\text{rel,vis}}^*} \right)^{1/4} \left(\frac{H_*/m}{0.2} \right) 10^{0.5 \log_{10}(m/m_0) - 1.75}, \quad (2.16)$$

where $g_{\text{rel,vis}}^*$ is the effective number of relativistic degrees of freedom in the visible sector.

3 Data analysis and results

In this section, we perform the cosmological parameter extraction. We first establish our data pipeline in Sec. 3.1 and then discuss the inclusion of ACT, SPT and BICEP data in sections 3.2, 3.3 and 3.4, respectively.

3.1 MCMC Analysis

For simulating the NEDE model, we employ the Boltzmann code `TriggerCLASS` (v. 4.0). Our MCMC analysis samples the six standard Λ CDM parameters (with flat priors and usual ranges): the baryon density $\Omega_b h^2$, the cold dark matter density $\Omega_c h^2$, the Hubble parameter H_0 , the amplitude $\log_{10}(10^{10} A_s)$ and scalar tilt n_s of the primordial spectrum, the reionization depth τ_{reio} and where applicable the tensor-to-scalar ratio r at a pivot scale of $k_* = 0.05 \text{ Mpc}^{-1}$. The neutrino sector is assumed to contain two massless and one massive species with $M_\nu = 3.046$. The Λ CDM parameter set is supplemented by the following cold NEDE parameters: the fraction of NEDE f_{NEDE} , the trigger mass $\log_{10}(m_\phi)$ (where $m_\phi \equiv m$ is measured in units of $1/\text{Mpc}$) and the equation of state of the NEDE fluid after the phase transition w_{NEDE}^* . We impose the respective prior ranges $0 < f_{\text{NEDE}} < 0.3$, $1.0 < \log_{10}(m_\phi) < 3.0$ and $1.0 < w_{\text{NEDE}}^* < 3.0$. The emergence of slight bimodalities within this 3-parameter NEDE model will motivate us to fix⁶ $w_{\text{NEDE}}^* = 2/3$ (we drop the asterisk henceforth for notational convenience) and study a 2-parameter NEDE model instead. In addition, we assume the rest-frame sound speed c_s^2 to equal the adiabatic sound speed defined in (2.11), thus $c_s^2 = w_{\text{NEDE}} = \text{const.}$ The trigger parameter is set to be $H_*/m_\phi = 0.2$, in accordance with a scalar field trigger that drops out of slow-roll as discussed in Sec. 2.

For the MCMC sampling we use `Cobaya` [56] and produce chains until the Gelman-Rubin criterion [57] satisfies $R - 1 < 0.01$, if not stated otherwise. For each run eight independent Markov chains are computed and can be publicly accessed⁷. Our combined analysis uses as a baseline the following likelihoods:

- Planck 2018 TT,TE,EE+lowE and lensing, with all nuisance parameters [58], (using v. 15.0 of `clik`⁸),
- BAO: 6dF 2011 + SDSS DR7&12 [59–61],
- Compilation of spectroscopically-confirmed SNe Ia, Pantheon [62],
- BBN: PArthENoPE [63].

We will join these base datasets with different combinations of the following datasets:

- **ACT:** The ACTpol DR4 power spectrum likelihood [64, 65]⁹. The data consists of measurements of the temperature and polarization CMB spectrum. It corresponds to the survey made between 2013 and 2016 at frequencies of 98 and 150 GHz and includes

⁶This bimodality was also observed previously by [38], who treated it by exploring two different regimes for the trigger mass.

⁷https://drive.google.com/drive/folders/1h_jwj1tFX1tcliToSLK0n891y9NH_y7q?usp=sharing

⁸<https://github.com/benabed/clik>

⁹<https://github.com/ACTCollaboration/pyactlike>

multipoles ranging from 600.5 to 7525.5 for the TT spectra and from 350.5 to 7525.5 for the TE/EE spectra. In order to avoid double counting and known tensions between Planck and ACT data, we follow the suggestion by the ACT collaboration and only include multipoles with $\ell > 1800$ when combined with the Planck likelihood.

- **SH₀ES:** We use the values reported in [6] and impose the following Gaussian prior on H_0 :

$$\chi_{H_0}^2 \equiv -2 \log \mathcal{L}_{H_0} = \left(\frac{H_0 - 73.04 \text{ km/s/Mpc}}{1.04 \text{ km/s/Mpc}} \right)^2. \quad (3.1)$$

- **SPT:** The SPT3G Y1[66] likelihood. The data corresponds to a solid angle of 1500 deg² and includes binned values for the EE and TE power spectra for the multipole range $300 \leq \ell < 3000$. It is reported by the SPT Collaboration that their best-fit parameter values are compatible with Λ CDM and their value of H_0 is compatible with the one deduced from Planck 2018.
- **BICEP:** The BICEP/Keck program consists of several millimeter wave receivers able to measure the B-mode components of the CMB polarization spectrum. An initial set of observations was made at 150 GHz over two years and has been supplemented in the following years starting in 2010. After a previous data release, aimed at collecting data around the 95 GHz band in 2014 and following one at 220 GHz in 2015, a more recent set of observations was made public. These data contains the observations done in 2016, 2017 and 2018 at 220GHz with which the tensor-to-scalar ratio, r , can be constrained even further. The data release, BICEP18, used in the present analyses covers an effective area of 600 square degrees at 95 GHz and 400 square degrees at 150 & 220 GHz and gives information at the multipole range $20 < \ell < 330$ [67].

As a first criterion to evaluate the model’s prospects, we compute the change in the effective chi-square, $\chi^2 = -2 \ln \mathcal{L}$ with \mathcal{L} being the model’s likelihood evaluated for the best-fit values, relative to the Λ CDM concordance model. We also report for each of the MCMC runs performed the absolute χ^2 values for each individual likelihood as well as for the total run. The remaining statistical discrepancy with respect to SH_0 ES, assuming Gaussian posteriors, can also be found in the corresponding tables.

Additionally, given that the Hubble tension is solely driven by the SH_0 ES measurement among the datasets we used, a second useful criterion is that of the tension difference of the maximum a posteriori, Q_{dmap} , advocated for in [12, 68]. It quantifies how much the quality of a given fit changes when the SH_0 ES likelihood is included. For a given dataset combination \mathcal{M} , it is defined as

$$Q_{\text{dmap}} \equiv \sqrt{\chi_{\mathcal{M}+SH_0ES}^2 - \chi_{\mathcal{M}}^2}, \quad (3.2)$$

and is expected to reduce to the normal tension measure if the posteriors are Gaussian. Most crucially, it can be applied in situations where the posteriors are non-Gaussian as in the case of NEDE. Intuitively, it tries to capture the idea that the “true” model should see the “true” physics even without SH_0 ES and hence minimize Q_{dmap} . In addition, we will also state the conventional Gaussian tension.

3.2 Study of NEDE including ACT

Here, we will study how NEDE reacts to including additional CMB temperature and polarization data from ACT. First, in Sec. 3.2.1, we will find that including ACT data leads to a bi-modality when fitting to the 3-parameter NEDE model. We will therefore propose a prescription to isolate the dominant mode. This, in turn, motivates our 2-parameter baseline model that will be discussed in Sec. 3.2.2.

3.2.1 Establishing the Baseline Model

We first consider the 3-parameter NEDE model where w_{NEDE} is allowed to vary along with f_{NEDE} and $\log_{10}(m_\phi)$. This is a joint analysis using the base datasets together with ACT and $SH_0\text{ES}$. We present the triangle plot for this run for the NEDE parameters in Fig. 1. The corresponding mean and best-fit values are reported in Tab. 1. Further derived parameters can be found in the Appendix in Tab. 5

Quite remarkably, when compared with the corresponding ΛCDM fit in Tab. 8, there is a χ^2 improvement of around 20 units, and a nonzero fraction of the NEDE fluid ($f_{\text{NEDE}} > 0$) is favored with more than 3.5σ preference. Moreover, we obtain $H_0 = 71.2 \pm 0.9$ km/s/Mpc (and best-fit 71.50 km/s/Mpc), which is in agreement with previous studies and confirms that the NEDE model is able to reduce the Hubble tension significantly.

These initial results, albeit reproducing the evidence for NEDE seen in previous analyses without ACT [12, 25], have to be taken with a grain of salt. The reason is that the posteriors for w_{NEDE} and $\log_{10}(m_\phi)$ show a slight bi-modality (see Fig 1), giving (weak) statistical support for the presence of an additional high-mass / low- w_{NEDE} mode at $w_{\text{NEDE}} \approx 1/3$ and $\log_{10}(m_\phi) \approx 3$ (corresponding to $z_* \approx 9000$). This questions the reliability of a conventional parameter extraction which generically assumes single-mode posteriors. As we will see, it also leads to an understatement of the model’s performance as a solution to the Hubble tension. Nevertheless, the observed bi-modality does not prevent the MCMC chains from converging using the standard sampling, and the dominant mode seems to be robust enough. For models with several equally strong modes, a nested sampler may be considered, but we deem this is not necessary for NEDE at this stage. We will, however, seek to confirm these conclusions in a future publication making use of a complementary approach using profile likelihoods as a way to deal with bimodalities (see [69] and for recent work in the context of EDE also [70]). Here, we will take another less computationally heavy path and fix $w_{\text{NEDE}} = 2/3$. It can be seen from Fig. 1 that this value corresponds to the dominant mode, in agreement with previous findings in the literature [38]. Moreover, for this mode, also the other model parameters remain consistent with the values obtained in a previous analysis without ACT. In particular, besides the shift in H_0 , we find an increase in ω_c , σ_8 and n_s (with relevance for inflationary model building), which is typical for models that feature an early dark energy component.

3.2.2 Results and Discussion

We present the posterior means with their 1σ confidence intervals and best-fit values for the 2-parameter NEDE model (with $w_{\text{NEDE}} = 2/3$) in Tab. 2, along with their corresponding $\Delta\chi^2$ and Q_{dmap} tension. Our main findings with regards to the Hubble tension are summarized in Fig. 2, depicting the f_{NEDE} vs H_0 contours. For completeness, the covariance contours for the six ΛCDM parameters can be found in Fig. 8 in the appendix. There, we also state the values of the different derived parameters (see Tab. A), and display the individual χ^2 per dataset (see Tab. 11 and Tab. 12 for ΛCDM and NEDE, respectively).

As a first sanity check, we use the baseline dataset with and without $SH_0\text{ES}$ to re-derive the results obtained in [25], this time with the Cobaya pipeline as described above (the old analysis used MontePython). We find that the extracted parameters deviate less than 0.5σ from their previously derived counterparts. In particular, with $SH_0\text{ES}$ included, there is a fit improvement over ΛCDM of $\Delta\chi^2 = -15.9$, and we have a sizable fraction of NEDE ($f_{\text{NEDE}} = 13.3 \pm 2.6\%$) that is accompanied by an increased value $H_0 = 71.7 \pm 0.8$ km/s/Mpc, reducing the Q_{dmap} tension below 2σ (down from 4.8σ in ΛCDM) in agreement with the findings in [12] (see also blue contour in Fig. 2). We further observe a 2.5% increase in n_s (and a milder increase in the spectral amplitude) when comparing with the corresponding ΛCDM run. As mentioned before in Sec. 3.2.2 this change is required to counter the gravitational effect of the dark sector acoustic oscillations that are typical for early dark energy models.

Name	Best-fit Mean _{Upper} Lower
$\Omega_b h^2$	0.023 0.022693 \pm 0.000185
$\Omega_c h^2$	0.130 0.12840 \pm 0.00303
H_0	71.502 71.230 \pm 0.890
$\log(10^{10} A_s)$	3.083 3.0702 \pm 0.0141
n_s	0.988 0.98855 ^{+0.00645} _{-0.00568}
τ_{reio}	0.054 0.05607 \pm 0.00715
f_{NEDE}	0.120 0.1093 ^{+0.0311} _{-0.0246}
$\log_{10}(m_\phi/\text{Mpc}^{-1})$	2.459 2.444 ^{+0.131} _{-0.112}
$3\omega_{\text{NEDE}}$	1.902 1.974 ^{+0.157} _{-0.202}
m_ϕ [Mpc ⁻¹]	287.950 302 ⁺⁵⁰ ₋₁₀₀
z_{decay}	4290.739 4322 ⁺⁶⁰⁰ ₋₈₀₀
$\sum \chi^2$	4044.31
$\Delta\chi^2$	-20.63

Table 1. Posterior means, 1σ confidence intervals and best-fit values for the MCMC simulation using the base datasets + ACT + SH_0 ES for the 3-parameter NEDE model, allowing sampling over w_{NEDE} . Shaded in gray are the NEDE-specific parameters together with the derived parameters m_ϕ and z_* . NEDE is preferred over Λ CDM with a significance of more than 3.5σ .

It is typically observed that without including SH_0 ES the evidence for NEDE seems much smaller (although the data fit still improves by $\Delta\chi^2 = -1.8$). By now, the reason for this has been investigated in detail by different authors [25, 27, 70, 71]: when the sampling algorithm probes smaller values of f_{NEDE} – as expected for a run without the statistical pull of the SH_0 ES dataset – the other NEDE parameter $\log_{10}(m_\phi)$ (or z_* equivalently) becomes less constrained (obviously, if there is only a small energy injection it does not matter when it happens). This corresponds to an increase in the overall sampling volume as $f_{\text{NEDE}} \rightarrow 0$ which makes the MCMC chain collect more data points in the low- f_{NEDE} region. This can be diagnosed independently through a non-Gaussian posterior for f_{NEDE} , which rather generically suggests a strong and unphysical prior dependence.

We now turn to the ACT runs and first investigate them in the absence of the SH_0 ES prior on H_0 . Figure 2 shows how the NEDE fit to the baseline datasets, and ACT is still affected by the before-mentioned sampling issues near the lower values of f_{NEDE} , which is evident by the enlargement and widening of the 68% C.L. towards the bottom. To confirm that this is indeed a sampling issue and still be able to extract cosmological parameters, we perform one run where we fix the mass of the trigger field to its best-fit value as given by the unrestricted simulation to obtain the green contours. As a result, we indeed find that the green relative to the purple contour moves to larger values of f_{NEDE} and, in fact, shows weak evidence for non-zero f_{NEDE} (with 1σ significance). Even more important is the observation

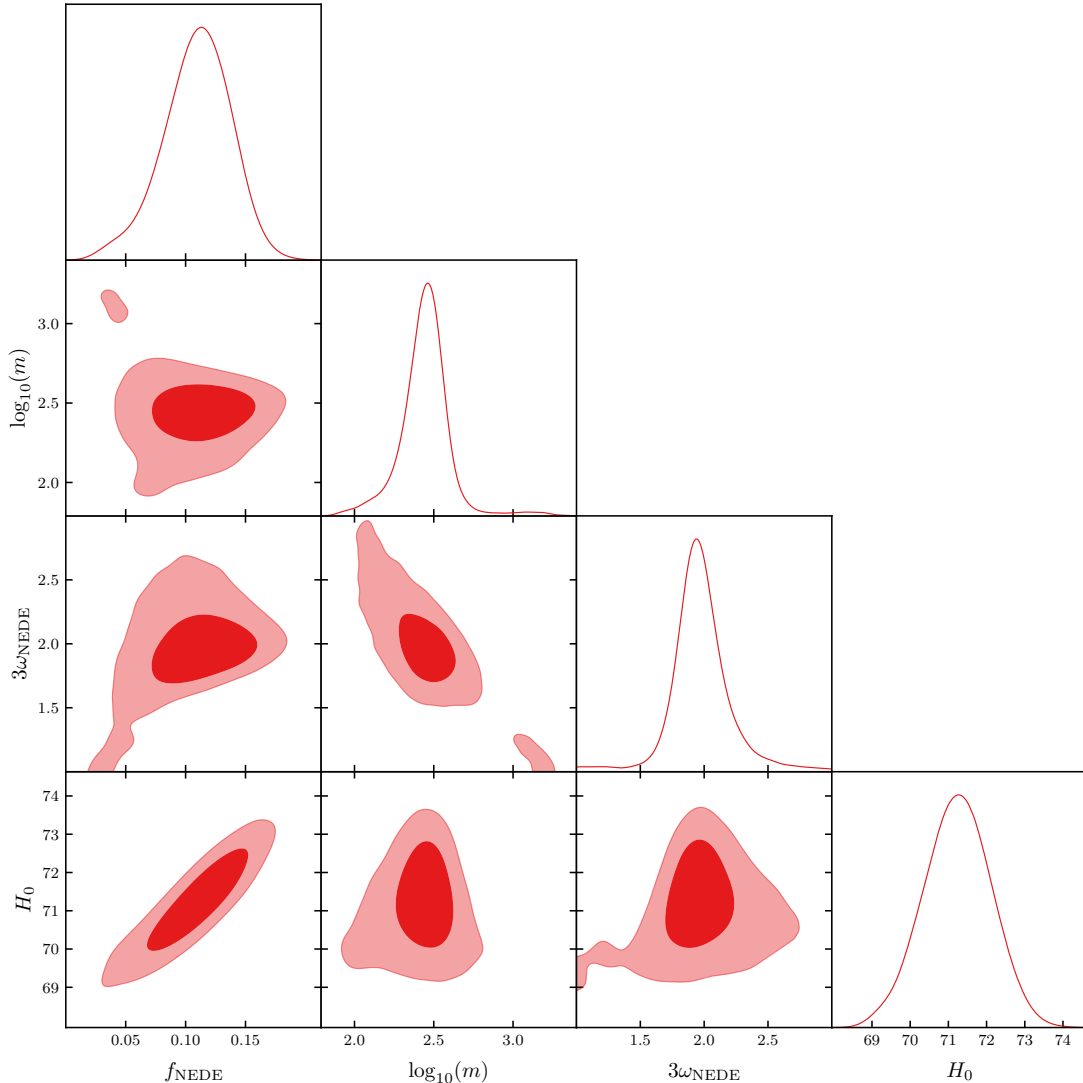


Figure 1. (Left) Covariances and posteriors for joint analysis of the base datasets with ACT and SH_0ES . There is a slight bi-modality: besides the dominant mode that shows typical NEDE behavior, there is weak evidence for a high-mass / low- w_{NEDE} mode. Later we choose the dominant mode by fixing $w_{NEDE} = 2/3$.

that NEDE makes the joint baseline and ACT datasets compatible with SH_0ES at the 95% C.L., which motivates the subsequent inclusion of the SH_0ES prior on H_0 .

Concerning the best-fit of the run including ACT (but without SH_0ES) there is some spurious improvement in χ^2 for fixed mass compared to the one with unconstrained mass due NEDE featuring approximately degenerate minima or flat directions in that region of parameter space. We performed different minimization procedures, which led to very similar values of χ^2 but still with some small variability in the cosmological parameters, however, all are compatible with the results for the posteriors.

In a nutshell, including ACT data in the presence of SH_0ES reproduces the baseline results qualitatively but leads to slightly weaker evidence for NEDE (compare the blue and red contour in Fig. 2). As usual, with the SH_0ES prior higher fractions of NEDE are favored; although, when also including ACT, f_{NEDE} is lower by $\simeq 1.4\%$ as compared to the run without ACT. Specifically, we can see from Tab. 2 that the central value lies at around a 12% fraction of NEDE and is favored over a null fraction by about 4.8σ . Without ACT we found a fraction of NEDE of around 13% with a 5.2σ preference over the null hypothesis.

We now highlight some of the remarkable features of the joint ACT analysis. The first

Parameter Name	NEDE fixed EOS				
	Base	+ACT	+ SH_0ES21	+ACT + SH_0ES21	+ACT fixed m_ϕ
$\Omega_b h^2$	0.023 $0.0226^{+0.00020}_{-0.00025}$	0.022 0.0225 ± 0.00019	0.023 0.0230 ± 0.00022	0.023 0.0227 ± 0.00017	0.023 0.0226 ± 0.00015
$\Omega_c h^2$	0.125 $0.1244^{+0.0025}_{-0.0048}$	0.124 $0.1230^{+0.0021}_{-0.0039}$	0.131 0.1308 ± 0.00301	0.131 0.1293 ± 0.00284	0.129 $0.1251^{+0.0028}_{-0.0036}$
H_0	69.444 $69.306^{+0.883}_{-1.48}$	69.015 $68.945^{+0.746}_{-1.34}$	71.759 71.698 ± 0.801	72.086 71.485 ± 0.822	70.955 $69.679^{+0.940}_{-1.25}$
$\log(10^{10} A_s)$	3.047 3.056 ± 0.0155	3.064 3.0577 ± 0.0141	3.065 3.0688 ± 0.0146	3.084 3.0710 ± 0.0144	3.078 3.0620 ± 0.0148
n_s	0.978 $0.9765^{+0.0069}_{-0.0093}$	0.976 $0.9757^{+0.0066}_{-0.0084}$	0.991 0.9910 ± 0.0057	0.995 $0.9905^{+0.0061}_{-0.0054}$	0.986 $0.9810^{+0.0063}_{-0.0075}$
τ_{reio}	0.055 0.0564 ± 0.0073	0.050 $0.0547^{+0.0064}_{-0.0073}$	0.054 0.0575 ± 0.0074	0.059 0.0559 ± 0.0073	0.053 0.0548 ± 0.0072
f_{NEDE}	0.067 < 0.132	0.053 < 0.107	0.135 0.1330 ± 0.0255	0.139 $0.119^{+0.0265}_{-0.0229}$	0.110 $0.0690^{+0.0326}_{-0.0370}$
$\log_{10} \left(\frac{m_\phi}{\text{Mpc}^{-1}} \right)$	2.543 2.554 ± 0.286	2.458 $2.313^{+0.427}_{-0.158}$	2.583 2.553 ± 0.100	2.468 $2.445^{+0.105}_{-0.0800}$	2.4583 –
m_ϕ [Mpc $^{-1}$]	349.486 < 1090	287.333 < 709	382.974 367^{+70}_{-90}	293.758 286^{+60}_{-60}	287.333 –
z_*	4881.454 5270^{+1000}_{-2000}	4397.410 4107^{+1000}_{-3000}	5007.738 4856^{+600}_{-600}	4306.963 4247 ± 600	4301.678 4370^{+63}_{-52}
Total χ^2	3804.26	4040.56	3806.74	4049.05	4039.26
$\Delta\chi^2$	–3.19	–1.82	–23.32	–15.89	–3.13
H_0 Tension	2.3σ	2.7σ	–	–	2.2σ
Q_{dmap}	–	–	1.57σ	2.9σ	–

Table 2. Best-fit results of the MCMC analysis involving the ACT data and pertinent likelihood combinations for reference. Colors correspond to the contours of Fig. 2. If only a one-sided constraint exists at 95%CL, it is given in the table instead of the 68% error.

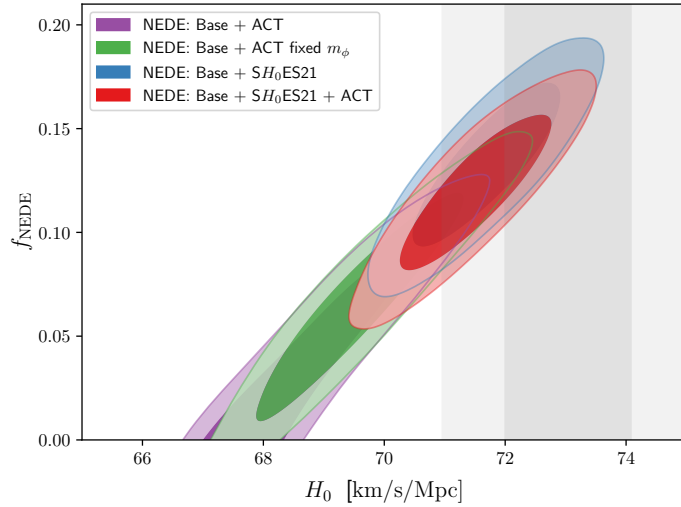


Figure 2. Covariance between f_{NEDE} and H_0 for different dataset combinations featuring the new ACT dataset. The NEDE model is subject to a fixed equation of state $w_{\text{NEDE}} = 2/3$.

observation relates to Λ CDM, where we see that when comparing corresponding datasets, NEDE achieves a better fit by decreasing the χ^2 by more than 15 units for the full data combination. Secondly, compared with the baseline dataset, ACT seems to slightly reduce the mean NEDE fraction, although in a statistically insignificant way. Interestingly, the best-fit values remain high and unaffected by ACT, meaning that the distribution becomes less Gaussian. This best-fit value for the NEDE fraction comes at the price of a slight worsening of the fit compared to the same analysis without ACT. Third, we can have a look at the second criterion, the Q_{dmap} , which attempts to favor models which do not change much by the inclusion of local measurements. In this regard, we see that ACT worsens the Q_{dmap} which is interpreted as ACT enhancing the pull that the SH_0 ES likelihood has on the data.

As derived parameters we show the plots for H_0 against $S8$ and r_s^d in Fig. 3 and include the bands given by SH_0 ES 2021[6] and in the case of $S8$, also the bands from the cosmic shear combined analysis of KiDS+VIKING-450 and DES-Y1[72]¹⁰. The plots include the contours obtained for Λ CDM and clearly show how the NEDE model moves the contours towards the SH_0 ES band, however, at the same time, the tension with the low- z values for $S8$ is increased mildly. To be precise, NEDE sits on the edge of the 2σ region for $S8$ and does not improve on the existing tension. Some more comments on this are given in the conclusions.

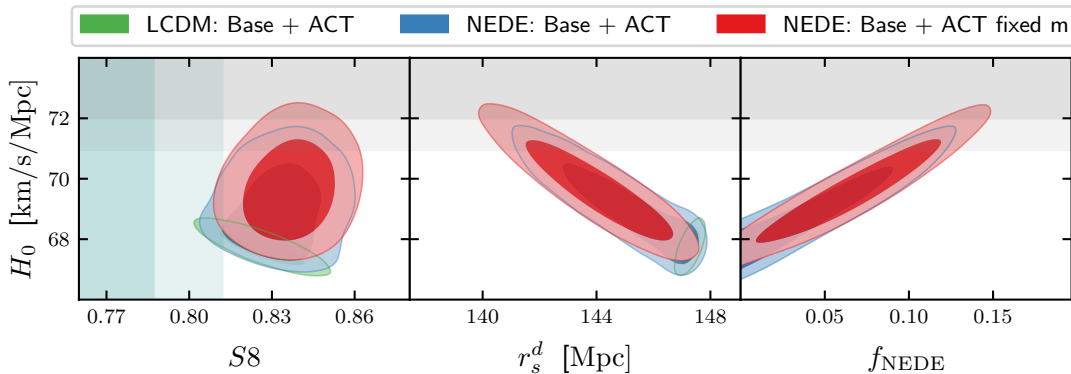


Figure 3. Plots showing the contours relating the Hubble parameter with $S8$, r_s^d and f_{NEDE} , while excluding the SH_0 ES likelihood. The gray bands show the 1 and 2σ contours coming from the latest SH_0 ES report [6], while the teal bands correspond to the measurements from KiDS+VIKING and DES [72].

3.3 Study of NEDE including SPT

Here, we perform similar joint analyses for the case of the SPT likelihood. The results for the best-fit values, posterior means, and 1σ confidence intervals are found in Table 3. A plot showing the covariance for H_0 against f_{NEDE} is given in Fig. 4. The full set of posteriors and marginalized distributions of the cosmological parameters shared with Λ CDM can be found in the triangle plot of Fig. 9. We include the results for some derived parameters in Table A and the χ^2 for the individual datasets for runs involving SPT in Tab. 13.

Let us make some observations regarding issues faced when performing MCMC analyses using the SPT likelihood. The sampling issues for low fractions of f_{NEDE} still persist when including SPT and excluding SH_0 ES, this can be seen from the non-vanishing left tail in the marginal f_{NEDE} distributions shown in Fig. 9 and from Fig. 4 where the contour of the run without fixing the trigger mass (purple) shows compatibility with vanishing f_{NEDE} while the run with fixed mass (green) reaches higher values. As discussed before, adapted sampling strategies are required to get rid of these spurious effects when sampling over all

¹⁰The newer data releases point at similar constraints but have not been combined yet: $S8 = 0.759^{+0.024}_{-0.021}$ [22] from KiDS - 1000 and $S8 = 0.772^{+0.018}_{-0.017}$ [73] from DES-Y3.

Parameter Name	NEDE fixed EOS				
	Base	+SPT	+ SH_0ES21	+SPT + SH_0ES21	+SPT fixed m_ϕ
$\Omega_b h^2$	0.023 $0.0227^{+0.00020}_{-0.00025}$	0.023 $0.0225^{+0.00016}_{-0.00020}$	0.023 0.0230 ± 0.00022	0.023 $0.0228^{+0.00017}_{-0.00020}$	0.023 0.0226 ± 0.00016
$\Omega_c h^2$	0.125 $0.1244^{+0.0025}_{-0.0048}$	0.125 $0.1233^{+0.0021}_{-0.0039}$	0.131 0.1308 ± 0.0030	0.129 0.1293 ± 0.0030	0.125 $0.1247^{+0.0027}_{-0.0037}$
H_0	69.444 $69.306^{+0.883}_{-1.48}$	69.319 $69.019^{+0.781}_{-1.27}$	71.759 71.698 ± 0.801	71.769 71.431 ± 0.852	69.461 $69.461^{+0.901}_{-1.26}$
$\log(10^{10} A_s)$	3.047 3.0560 ± 0.0155	3.055 3.0494 ± 0.0147	3.065 3.0688 ± 0.0146	3.071 3.0617 ± 0.0143	3.057 3.0513 ± 0.0147
n_s	0.978 $0.9765^{+0.0069}_{-0.0093}$	0.978 $0.9751^{+0.0062}_{-0.0080}$	0.991 0.9909 ± 0.0057	0.990 0.9888 ± 0.0059	0.978 $0.9784^{+0.0064}_{-0.0077}$
τ_{reio}	0.055 0.0564 ± 0.0073	0.055 0.0544 ± 0.0072	0.054 0.0575 ± 0.0074	0.061 0.0555 ± 0.0071	0.057 0.0542 ± 0.0070
f_{NEDE}	0.067 < 0.132	0.066 < 0.112	0.135 0.1330 ± 0.0255	0.126 $0.1212^{+0.0275}_{-0.0244}$	0.066 < 0.124
$\log_{10} \left(\frac{m_\phi}{\text{Mpc}^{-1}} \right)$	2.543 2.554 ± 0.286	2.496 $2.447^{+0.306}_{-0.168}$	2.583 2.553 ± 0.100	2.443 2.474 ± 0.113	2.496 –
$m_\phi [\text{Mpc}^{-1}]$	349.486 < 1090	313.191 < 745	382.974 367^{+70}_{-90}	277.137 308^{+50}_{-90}	313.191 –
z_*	4881.454 5270^{+1000}_{-2000}	4593.696 4640 ± 2000	5007.738 4856^{+600}_{-600}	4190.443 4417^{+500}_{-700}	4593.468 $4593.3^{+69.5}_{-52.1}$
Total χ^2	3804.27	4923.27	3806.74	4926.58	4923.22
$\Delta\chi^2$	-3.19	-3.32	-23.32	-23.13	-3.37
H_0 Tension	2.3 σ	2.7 σ	–	–	2.4 σ
Q_{dmap}			1.57 σ	1.82 σ	

Table 3. Table with the best-fit values followed by the posterior means and standard deviations of the Λ CDM and NEDE MCMC runs alternating datasets involving the baseline, SPT and SH_0ES . If only a one-sided constraint exists at 95%CL, it is given in the table instead of the 68% error. This way of reporting, however, hides the fact that for fixed m_ϕ we do find almost a 2 σ evidence for $f_{\text{NEDE}} = 6.6^{+3.2}_{-3.9}$ % even without SH_0ES , as further discussed in the text.

NEDE parameters. In any event, the crucial observation is that NEDE makes the datasets compatible with SH_0ES , corresponding to the green (and even purple) contour overlapping with the SH_0ES band within their respective 95% confidence limits. This, in turn, justifies a joint analysis with SH_0ES . On a cautionary note, given the number of nuisance parameters related to the SPT likelihood, convergence is particularly slow for these runs.

Overall, we obtain consistent features with what we have seen from the baseline datasets and from ACT in the previous subsection. It can be observed from the χ^2 values reported in Tab. 3, that the NEDE model presents an improvement in χ^2 for each combination of the datasets used. Most remarkable is the decrease of ~ 23 units (stronger than for ACT and similar to the baseline data) for the runs involving SPT and SH_0ES . As expected, NEDE manages to fit higher values of H_0 as can be seen from Fig. 4 which depicts the covariance contours for the different runs, including different combinations of SPT and SH_0ES . We, therefore, conclude that NEDE can also resolve the Hubble tension that arises between SH_0ES and the joint baseline (including Planck) and SPT data.

Including SPT has the effect of very slightly reducing the fraction of NEDE (by 1.2%), yielding $f_{\text{NEDE}} = 12.1^{+2.8}_{-2.4}$ % (as compared to $f_{\text{NEDE}} = 13.3 \pm 2.6$ %). This still supports

the existence of NEDE at $> 99.7\%$. The marginal difference between both runs is also apparent from the broad overlap of the red with the blue contour in Fig. 4, depicting the covariance between f_{NEDE} and H_0 . Similar insignificant changes occur for $\log_{10}(m_\phi)$ and H_0 . As discussed before, the addition of NEDE is known to increase the amount of cold dark matter, $\omega_c = \Omega_c h^2$, and to give higher values for the scalar spectral index, n_s . These qualitative features are left unchanged by the addition of SPT, giving $\omega_c = 0.129 \pm 0.003$ (Λ CDM: $\omega_c = 0.117 \pm 0.0008$) and $n_s = 0.989 \pm 0.006$ (Λ CDM: $n_s = 0.971 \pm 0.004$). For a more exhaustive comparison of the parameter contours against Λ CDM see Fig. 9 and for a comparison between SPT and ACT data within NEDE see Fig. 7. As can be seen, ACT and SPT have a similar and consistent impact on the f_{NEDE} posteriors.

Without including SH_0ES but keeping SPT, we get an improvement of 3.3 units in χ^2 when compared to a Λ CDM run with the same dataset combination and almost a 2σ evidence for $f_{\text{NEDE}} = 6.6^{+3.2}_{-3.9}\%$. As opposed to the ACT runs discussed previously, including SH_0ES yields a stronger improvement of 23 units, which is similar to the baseline result.

As mentioned before, adding SPT does not affect the model’s ability to address the Hubble tension, accordingly the Q_{dmap} tension remains below 2σ (changing only insignificantly by $< 0.3\sigma$).

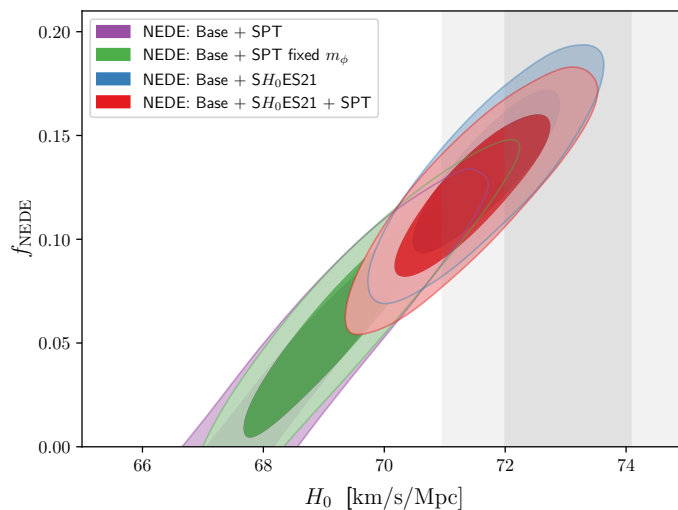


Figure 4. Plot of the covariance between f_{NEDE} and H_0 for different dataset combinations featuring the new SPT dataset. The NEDE model is subject to a fixed equation of state $w_{\text{NEDE}} = 2/3$.

As with ACT, we provide plots for H_0 against $S8$, r_s^d and f_{NEDE} for the datasets that involve SPT but exclude SH_0ES in Fig. 3.3. We see that the NEDE contour overlaps separately with both the $S8$ and SH_0ES constraint at 95% C.L.. However, we also see that there is only a very marginal common overlap between all three contours. This means that NEDE (in its current form) cannot solve both tensions simultaneously.

3.4 Consequences for Inflation using BICEP

In order to explain the homogeneity, isotropy, and flatness of the observed Universe, an epoch of cosmological inflation has been added to the Λ CDM model as suggested in the early 80’s [47, 74, 75]. Since then, many variants and models specifying the details of how this epoch transpired have been proposed. They can be broadly classified into two categories according to the number of additional fields required in a given inflationary model. In the simplest cases, i.e. for any model that implements inflation by means of a single additional field, it is possible to compute the predicted primordial power spectrum and constrain n_s , the scalar spectral tilt, and r , the tensor-to-scalar ratio.

With ongoing experiments such as Planck [76] and the BICEP3/Keck Array [67], n_s and r can be constrained once a cosmological model is assumed. While Planck measures

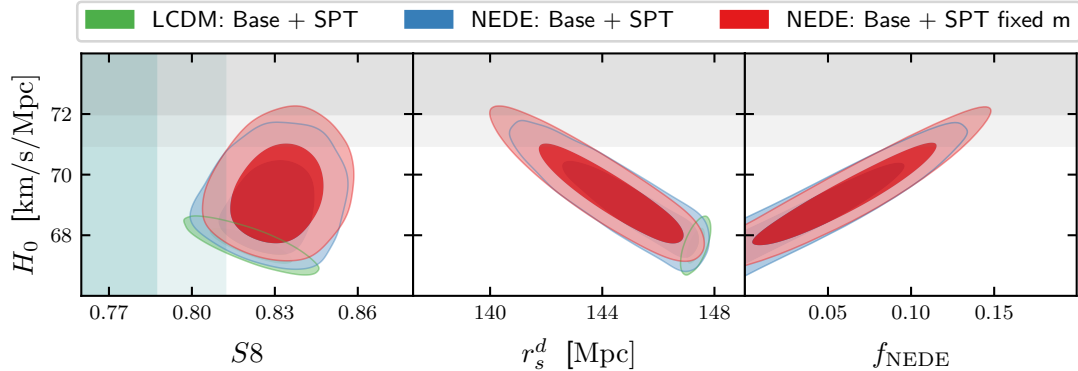


Figure 5. Plots showing the contours relating the Hubble parameter with $S8$, r_s^d and f_{NEDE} as obtained when including SPT data while excluding the $SH_0\text{ES}$ likelihood. The gray bands show the 1 and 2σ contours coming from the latest $SH_0\text{ES}$ reports [6], while the teal bands correspond to the measurements from KiDS+VIKING and DES [72].

the whole sky, BICEP3 focuses on smaller low-foreground patches of the sky and achieves higher sensitivity. Most inflationary models can be constrained by the parameters n_s and r , this is, in particular, true for single-field models observing the slow-roll single-field condition. At present, Starobinsky inflation [47], or R^2 inflation, predicts values that are in very good agreement with ΛCDM , while many other models for inflation are believed to be excluded given the amount of confidence in the standard model of cosmology – ΛCDM .

For the reasons above, it is extremely important to update these constraints in view of the NEDE model. To that end, we perform an MCMC simulation to obtain the NEDE confidence contours in the $n_s - r$ plane. We employ the baseline datasets supplemented with $SH_0\text{ES}$ 2021 [6] and BICEP18 [67] and evaluate primordial quantities at the pivot scale $k_* = 0.05 \text{ Mpc}^{-1}$. We sample r while keeping the single-field consistency relation $n_t = -r/8$. We demand the sampling to reach a Gelman-Rubin criterion of $R - 1 < 0.05$. Our results are summarized in Fig. 6, which shows the 68% (dark shading) and 95% (light shading) C.L. of one ΛCDM (green) and two NEDE simulations (orange and blue) along with the predicted values and regions for some relevant models of inflation. Best-fit values, posterior means, and errors can be found in the Tab. 4.

Looking at Fig. 6, we observe that the effect of assuming NEDE is to shift the contours towards a bluer spectrum (or larger n_s equivalently). In particular, when considering the baseline dataset together with BICEP18 and $SH_0\text{ES}$, values of n_s very close to unity can be reached within 68% C.L.. While the current bounds on r exclude the simplest ϕ and ϕ^2 models of inflation, NEDE allows n_s to be higher and rescues models that have convex potentials, power-law inflation, or that alternatively, feature more than one field.

Besides the simpler ϕ^2 potential line (blue solid) and the convex line (black solid), we see that power-law inflation [77, 78] (green dashed) is again possible within the NEDE model. In such a case, the scale factor of the universe evolves following a power law and is implemented via a potential that is exponential, and in agreement with a nearly conformal initial state of the Universe [79].

It is worth looking at two-field models as well, in view of the NEDE posteriors presented in Fig. 6. An estimate of the contours shown has already appeared in the context of a two-stage monodromy inflation model [43], where these seem to be compatible with the first stage of inflation lasting about 55 to 60 e -folds. Along similar lines, multi-field models featuring an inflation together with a curvaton as proposed in [44–46], can cover a bigger piece of the parameter space for n_s and r , corresponding to the yellow shaded area in Fig. 6. Following the constraints in the general mixed inflaton-curvaton [80–84], we can estimate the number of e -folds and the η_σ parameter proportional to the curvaton’s mass for the mean values

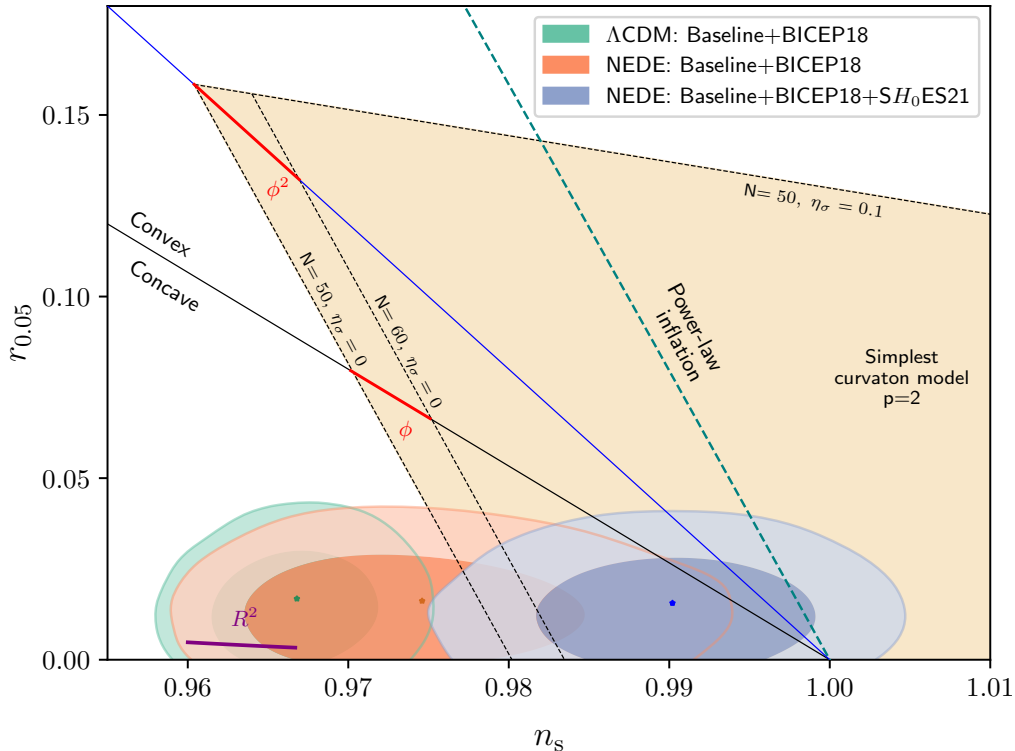


Figure 6. Results for the 68% and 95% C.L. contours relating n_s and r at a pivot scale of $k_* = 0.05$, for the Λ CDM and NEDE models alternating the baseline datasets with SH_0ES while including BICEP18. The small asterisks represent the mean posterior value of the corresponding contours.

produced by NEDE. For the case of the simplest curvaton model [85] one has that the scalar spectral tilt and the tensor-to-scalar ratio are given by

$$n_s = 1 - \frac{1}{1+R} \frac{2(2+p)}{4N+p} + \frac{R}{1+R} \left[-2\epsilon + 2\eta_\sigma \right], \quad (3.3a)$$

$$r = \frac{16\epsilon}{1+R}, \quad (3.3b)$$

$$m_\sigma = H_* \sqrt{3\eta_\sigma} \sim 10^{13} - 10^{14} \text{ GeV}, \quad (3.4)$$

depending on the number of e -folds chosen. Having an extra light scalar field, like the curvaton, with a mass within an order of magnitude of the Hubble scale during inflation does not add any additional fine-tuning or naturalness problems.

It is interesting to note that in the case of $r = 0$, the pure curvaton model predicts a testable level of local non-Gaussianity of $f_{\text{NL}} = -5/4$ [86], while for larger r , f_{NL} becomes proportionally smaller. Hence the tensor-to-scalar ratio and non-Gaussianity are complementary probes of the curvaton model.

4 Discussion and summary

We tested the NEDE model against additional CMB data arising from the ground-based experiments ACT, SPT, and BICEP3/Keck. We have observed in all three cases that the NEDE model maintains its ability to address the Hubble tension despite the additional constraining power of these datasets. In particular, we found that each ground-based experiment in combination with our baseline dataset, consisting of BAO, Pantheon and Planck data, prefers a non-vanishing fraction of NEDE with a significance larger than 4.5σ if we include a SH_0ES prior on H_0 . In all cases, this comes with a significantly reduced Hubble tension and a more than 4σ increase of the spectral tilt n_s as compared to its Λ CDM

Parameter Name	Λ CDM: Base + BICEP18	NEDE: Base + BICEP18	NEDE: Base + BICEP18 + SH_0 ES
$\Omega_b h^2$	0.022 0.0224 ± 0.00013	0.023 $0.0226^{+0.0002}_{-0.0003}$	0.023 0.0230 ± 0.0002
$\Omega_c h^2$	0.119 0.1193 ± 0.0009	0.124 $0.1233^{+0.0019}_{-0.0042}$	0.130 0.1299 ± 0.0032
H_0	67.680 67.688 ± 0.408	69.078 $68.963^{+0.720}_{-1.35}$	71.374 71.538 ± 0.864
$\log(10^{10} A_s)$	3.046 3.0487 ± 0.0142	3.063 3.0550 ± 0.0152	3.062 3.0685 ± 0.0147
n_s	0.965 0.9668 ± 0.0037	0.975 $0.9746^{+0.0060}_{-0.0089}$	0.988 0.9902 ± 0.0062
τ_{reio}	0.054 0.0569 ± 0.0072	0.057 0.0565 ± 0.0073	0.054 $0.0578^{+0.0069}_{-0.0076}$
$r_{0.05}$	0.000 < 0.0354	0.000 < 0.0344	0.000 < 0.0335
f_{NEDE}	– –	0.054 < 0.118	0.126 $0.129^{+0.030}_{-0.026}$
$\log_{10} \left(\frac{m_\phi}{\text{Mpc}^{-1}} \right)$	– –	2.568 $2.417^{+0.389}_{-0.173}$	2.527 $2.511^{+0.143}_{-0.097}$
$3\omega_{\text{NEDE}}$	– –	2.012 > 1.42	2.090 $2.119^{+0.120}_{-0.195}$
$m_\phi [\text{Mpc}^{-1}]$	– –	370.021 < 781	336.556 339^{+90}_{-100}
z_*	– –	5065.098 4569 ± 2000	4673.963 4633 ± 800

Table 4. Best-fit values, means and 1σ confidence intervals for MCMC runs involving the BICEP18 dataset, together with their corresponding χ^2 individual and total values.

value. Overall, we find that the extracted parameter values are fully compatible with the ones obtained by only using CMB data from Planck. This is emphatically summarized in Fig. 7.

In a first series of simulations, we have examined the effects of including the CMB likelihood from ACT. We first recovered a slight bi-modality in the three-parameter NEDE model that had previously been reported in [38]. This is in general a challenge for sampling algorithms and we dealt with it by choosing the dominant mode centered around an equation of state parameter $w_{\text{NEDE}} = 2/3$. This value falls within the theoretically allowed regime and corresponds to a bubble wall condensate that decays quicker than the dominant radiation component. In the presence of ACT, this two-parameter model was found to make the inferred value of H_0 compatible with the SH_0 ES value, motivating a combined analysis with SH_0 ES. In this case, we report 71.49 ± 0.822 km/s/Mpc (68% C.L.) and a best-fit of $H_0 = 72.09$ km/s/Mpc. The fit quality compared to Λ CDM improves significantly by $\Delta\chi^2 = -15.9$, albeit less pronounced than without ACT ($\Delta\chi^2 = -23.3$). This corresponds to a reduced Q_{dmap} tension of 2.9σ down from 4.8σ within Λ CDM, which should be compared with a tension of 1.6σ for the baseline dataset. We therefore conclude that ACT data makes NEDE somewhat less efficient at addressing the Hubble tension, although the evidence for

NEDE remains with 4.7σ high. At this stage, it remains to be seen whether this observation is supported by future data releases.

With SPT things are even simpler. Both the posteriors and the χ^2 improvement over Λ CDM only change slightly compared to the baseline runs. For completeness, we find 71.431 ± 0.852 km/s/Mpc (68% C.L.) and a best-fit of $H_0 = 71.77$ km/s/Mpc along with a strong fit corresponding to $\Delta\chi^2 = -23.1$. Moreover, the Q_{dmap} remains below 2σ . We stress that this outcome, while it might appear uneventful, is important news for NEDE. After all, CMB data is the best probe we have to test the model. It also puts the marginally weaker ACT outcome into perspective and highlights the relevance of testing the model with different probes.

Our analysis also shows that both ACT and SPT data do not yet have the constraining power to strengthen (or weaken) the evidence for NEDE. We expect this conclusion to change with future data. Also the situation with $S8$ remains unchanged. NEDE in its current form does not improve on the issue, while also not making it much worse compared to Λ CDM. Here, progress might come from two directions: First, with Hot NEDE [33, 34] there is a new microscopic implementation of NEDE that contains a richer dark sector that is also expected to change the prediction for $S8$. Alternatively, given that the tension is mild, there is still the possibility of systematics explaining the data. For example, there are hints from the James Webb Space Telescope indicating anomalies within Λ CDM, which themselves may point towards a higher $S8$ [87]. Moreover, possible systematic issues in the lensing and clustering probes are currently being studied [88] and may still have something to say about $S8$.

Finally, we also explored the relevance of our findings for inflation. Specifically, we supplemented our analysis with BICEP3/Keck data to constrain the tensor-to-scalar ratio and create an updated version of the r vs n_s plot, which is the main phenomenological input for inflationary model building. In agreement with a previous statement in the literature [25, 43], we find that NEDE prefers a significantly bluer spectrum, $n_s = 0.9902 \pm 0.006$. If this result stands the test of time, it will have dramatic consequences for our understanding of the primordial universe. Specifically, it implies that Starobinsky’s model is no longer a good fit to the data. Instead, the simplest curvaton model would provide a better explanation for the initial conditions of the Universe in agreement with NEDE as a solution to the Hubble tension.

Acknowledgements

We would like to thank Guido D’Amico, Nemanja Kaloper, Antony Lewis, Vivian Poulin, Toni Riotto, and Jussi Valiviita for useful discussions. This work is supported by Independent Research Fund Denmark grant 0135-00378B.

A Complementary results for MCMC analyses of the different runs

Simulations were all made with fixed EOS and for the following combinations of likelihoods:

- R1 - NEDE: Baseline
- R2 - NEDE: Baseline + ACT
- R3 - NEDE: Baseline + SH_0ES21
- R4 - NEDE: Baseline + ACT + SH_0ES21
- R5 - NEDE: Baseline + ACT fixed m to best-fit of R2

Posterior mean values and the 68.27% confidence intervals for the set of runs involving the SPT data

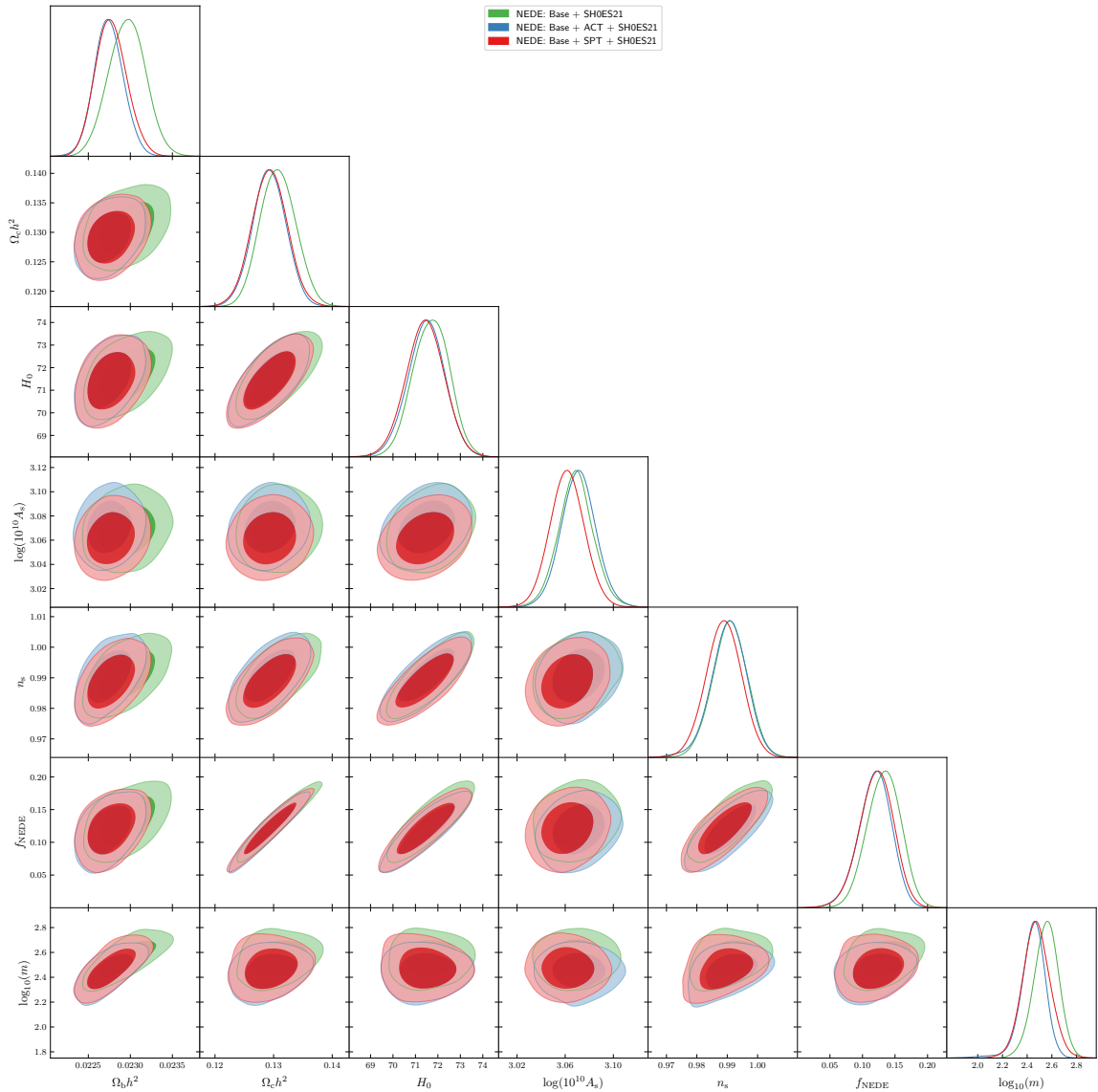


Figure 7. Contour plots for some of the parameters sampled in the NEDE model. The two sets of contours show the impact of SPT and ACT on the predicted cosmological parameter posteriors for the NEDE model. Overall, adding these additional datasets leads to only small changes.

Parameter Name	Mean and Std. Dev.	Best-fit
Ω_m	0.2991 ± 0.0051	0.299
$\Omega_m h^2$	0.1517 ± 0.0031	0.1529
Ω_Λ	0.7008 ± 0.0051	0.7009
σ_8	0.8386 ± 0.0096	0.8461
$\sigma_8/h^{0.5}$	0.9936 ± 0.0087	1.0007
$\sigma_8 \Omega_m^{0.5}$	0.4586 ± 0.0065	0.4627
$\sigma_8 \Omega_m^{0.25}$	0.6201 ± 0.0075	0.6257
Age/Gyr	$13.24^{+0.13}_{-0.15}$	13.19
r_s^d	$142.0^{+1.37}_{-1.57}$	141.46

Table 5. Posterior mean and standard deviation for some derived parameters of the run described in Sec. 3.1 having an unconstrained equation of state.

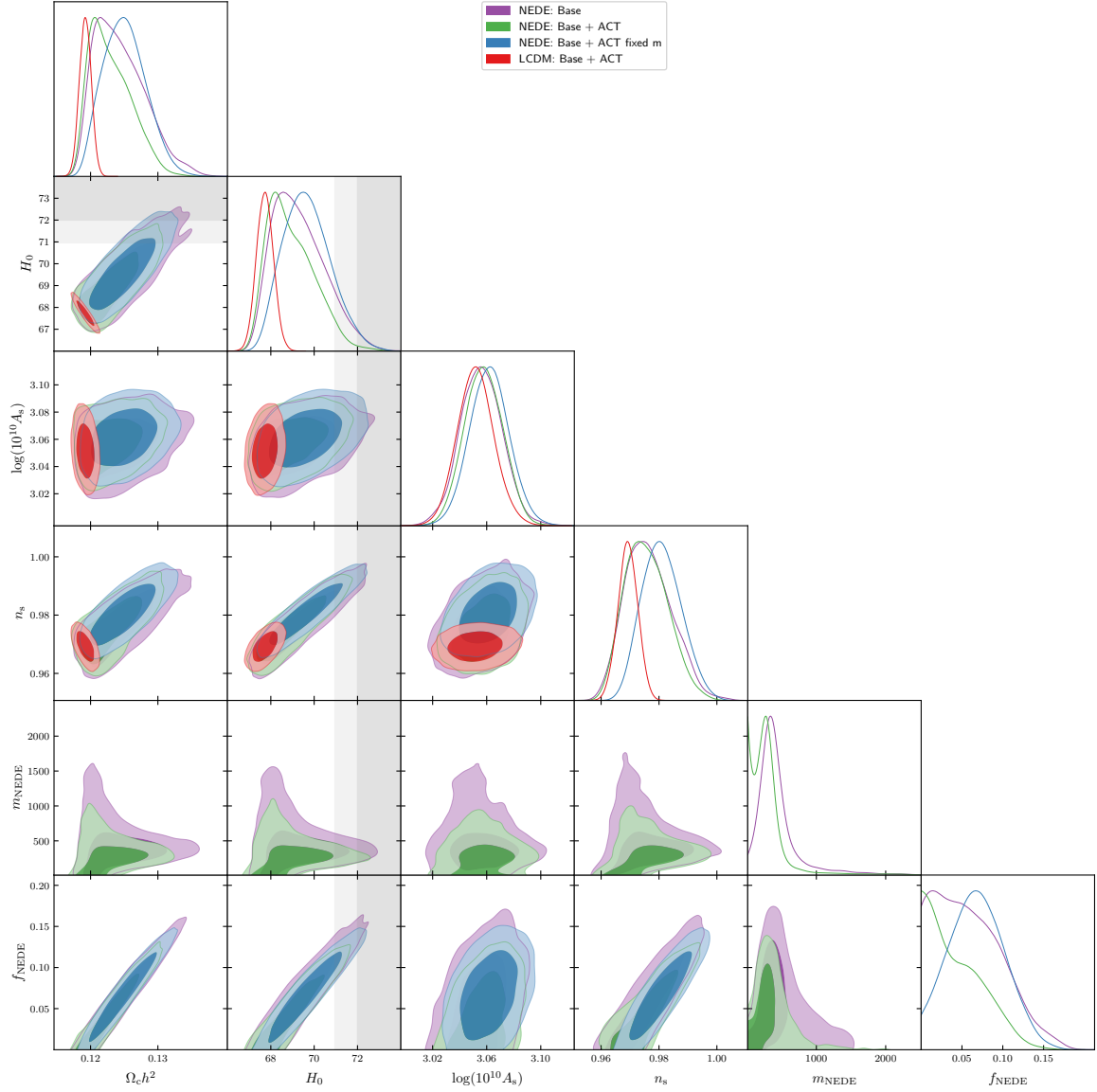


Figure 8. Triangle plot displaying the original six parameters of Λ CDM and their 68% and 95% C.L. contours coming out of the MCMC analysis of Λ CDM and the NEDE models, highlighting the impact of the ACT dataset on the fits, described in subsection 3.2.

Name	R1 - Mean _{Lower} ^{Upper}	R2 - Mean _{Lower} ^{Upper}	R3 - Mean _{Lower} ^{Upper}	R4 - Mean _{Lower} ^{Upper}	R5 - Mean _{Lower} ^{Upper}
Ω_m	0.3075 ± 0.0061	0.3074 ± 0.0059	0.3003 ± 0.0051	0.2987 ± 0.0050	0.3055 ± 0.0057
$\Omega_m h^2$	$0.1477^{+0.0026}_{-0.0050}$	$0.1461^{+0.00212}_{-0.0041}$	0.1544 ± 0.0031	0.1527 ± 0.0029	$0.1483^{+0.0029}_{-0.0037}$
Ω_Λ	0.6924 ± 0.0061	0.6925 ± 0.0059	0.6996 ± 0.0051	0.7012 ± 0.0050	0.6944 ± 0.0057
z_{re}	7.905 ± 0.726	7.744 ± 0.703	8.068 ± 0.734	7.927 ± 0.738	7.769 ± 0.725
σ_8	$0.8237^{+0.0095}_{-0.013}$	$0.8225^{+0.0084}_{-0.012}$	0.8415 ± 0.0092	0.8408 ± 0.0092	$0.8291^{+0.0096}_{-0.011}$
$\sigma_8/h^{0.5}$	0.9895 ± 0.0091	0.9906 ± 0.0084	0.9938 ± 0.0088	0.9945 ± 0.0087	0.9933 ± 0.0084
$\sigma_8 \Omega_m^{0.5}$	0.4568 ± 0.0070	0.4560 ± 0.0062	0.4611 ± 0.0067	0.4595 ± 0.0064	0.4583 ± 0.0061
$\sigma_8 \Omega_m^{0.25}$	$0.6134^{+0.0076}_{-0.0093}$	$0.6124^{+0.0068}_{-0.0080}$	0.6229 ± 0.0075	0.6216 ± 0.0073	0.6164 ± 0.0073
Age/Gyr	$13.5^{+0.255}_{-0.117}$	$13.6^{+0.216}_{-0.090}$	13.1 ± 0.127	$13.2^{+0.118}_{-0.131}$	$13.5^{+0.188}_{-0.148}$
r_s^d	$144.3^{+2.65}_{-1.23}$	$145.2^{+2.20}_{-0.98}$	140.73 ± 1.40	141.54 ± 1.36	$144.0^{+1.88}_{-1.53}$

Table 6. Posterior means for some derived parameters in the NEDE MCMC simulations for different combinations of datasets involving the baseline, ACT and SH_0ES , with a fixed EOS to $\omega_{NEDE} = 2/3$.

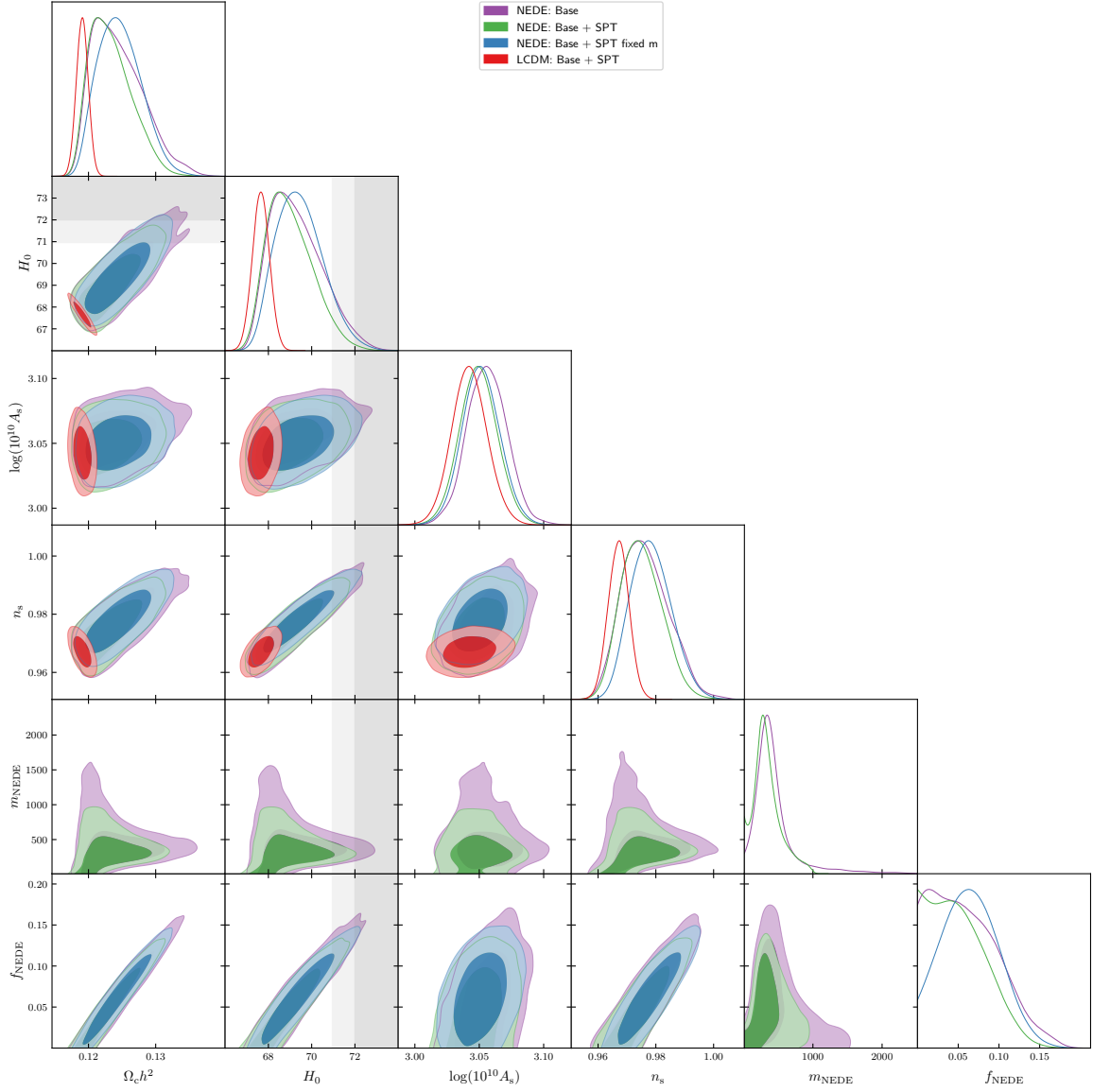


Figure 9. Triangle plot displaying the original six parameters of Λ CDM and their 68% and 95% C.L. contours coming out of the MCMC analysis of Λ CDM and the NEDE models, highlighting the impact of the SPT dataset on the fits. This set of simulations is described in subsection 3.3.

- S1 - Λ CDM: Planck BAO SN SPT
- S2 - NEDE: Baseline + SPT fixed EOS
- S3 - NEDE: Baseline + SH_0 ES
- S4 - NEDE: Baseline + SPT fixed EOS + SH_0 ES
- S5 - NEDE: Baseline + SPT fixed EOS fixed m_ϕ to best-fit of S2

B Individual χ^2 for the different chains presented

References

- [1] S. Nadathur, W.J. Percival, F. Beutler and H.A. Winther, *Testing Low-Redshift Cosmic Acceleration with Large-Scale Structure*, *Phys. Rev. Lett.* **124** (2020) 221301.

Name	S1 - Mean ^{Upper} _{Lower}	S2 - Mean ^{Upper} _{Lower}	S3 - Mean ^{Upper} _{Lower}	S4 - Mean ^{Upper} _{Lower}	S5 - Mean ^{Upper} _{Lower}
Ω_m	0.3105 ± 0.0053	0.3077 ± 0.0059	0.3003 ± 0.0051	0.2994 ± 0.0052	0.3066 ± 0.0057
$\Omega_m h^2$	0.1421 ± 0.0009	$0.1465^{+0.0021}_{-0.0041}$	0.1544 ± 0.0031	0.1527 ± 0.0031	$0.1479^{+0.0028}_{-0.0039}$
Ω_Λ	0.6894 ± 0.0053	0.6923 ± 0.0059	0.6996 ± 0.0051	0.7006 ± 0.0052	0.6933 ± 0.0057
z_{re}	7.687 ± 0.706	7.708 ± 0.723	8.068 ± 0.73	7.885 ± 0.721	7.697 ± 0.72
σ_8	0.8075 ± 0.0057	$0.8188^{+0.0084}_{-0.011}$	0.8415 ± 0.0092	0.8357 ± 0.0092	$0.8227^{+0.0090}_{-0.011}$
$\sigma_8/h^{0.5}$	0.9818 ± 0.0079	0.9856 ± 0.0084	0.9938 ± 0.0088	0.9888 ± 0.0085	0.9871 ± 0.0084
$\sigma_8 \Omega_m^{0.5}$	0.4500 ± 0.0054	0.4541 ± 0.0062	0.4611 ± 0.0067	0.4572 ± 0.0064	0.4555 ± 0.0061
$\sigma_8 \Omega_m^{0.25}$	0.6028 ± 0.0054	$0.6098^{+0.0068}_{-0.0077}$	0.6229 ± 0.0075	0.6181 ± 0.0073	0.6122 ± 0.0073
Age/Gyr	13.80 ± 0.018	$13.56^{+0.22}_{-0.094}$	13.14 ± 0.13	13.20 ± 0.132	$13.49^{+0.197}_{-0.143}$
r_s^d	147.3 ± 0.22	$144.9^{+2.25}_{-1.00}$	140.7 ± 1.40	141.5 ± 1.42	$144.2^{+1.98}_{-1.48}$

Table 7. Table displaying the posterior means and standard deviations for some derived parameters of the runs involving the SPT likelihood.

Parameter Name	Λ CDM (Base = Planck+BAO+SN)					
	Base	+ACT	+SPT	+SH ₀ ES	+ACT +SH ₀ ES21	+SPT +SH ₀ ES21
$\Omega_b h^2$	0.022	0.022	0.022	0.023	0.022	0.023
$\Omega_c h^2$	0.119	0.119	0.119	0.117	0.118	0.118
H_0	67.643	67.817	67.747	68.630	68.242	68.361
$\log(10^{10} A_s)$	3.052	3.067	3.038	3.061	3.073	3.059
n_s	0.966	0.968	0.967	0.971	0.971	0.972
τ_{reio}	0.058	0.057	0.052	0.062	0.060	0.061
Total χ^2	3807.45	4042.38	4926.59	3830.06	4064.94	4949.71
Q_{dmap}		—		4.75σ	4.75σ	4.75σ

Table 8. Best-fit results of the MCMC analysis for Λ CDM involving the ACT data and pertinent likelihood combinations for reference.

- [2] E. Abdalla et al., *Cosmology intertwined: A review of the particle physics, astrophysics, and cosmology associated with the cosmological tensions and anomalies*, *JHEAp* **34** (2022) 49 [2203.06142].
- [3] L. Knox and M. Millea, *Hubble constant hunter’s guide*, *Phys. Rev. D* **101** (2020) 043533 [1908.03663].
- [4] E. Di Valentino et al., *Snowmass2021 - Letter of interest cosmology intertwined II: The hubble constant tension*, *Astropart. Phys.* **131** (2021) 102605 [2008.11284].
- [5] PLANCK collaboration, *Planck 2018 results. VI. Cosmological parameters*, *Astron. Astrophys.* **641** (2020) A6 [1807.06209].
- [6] A.G. Riess et al., *A Comprehensive Measurement of the Local Value of the Hubble Constant with 1 km s⁻¹ Mpc⁻¹ Uncertainty from the Hubble Space Telescope and the SH0ES Team*, *Astrophys. J. Lett.* **934** (2022) L7 [2112.04510].
- [7] R. Wojtak, A. Knebe, W.A. Watson, I.T. Iliev, S. Heß, D. Rapetti et al., *Cosmic variance of the local Hubble flow in large-scale cosmological simulations*, *Mon. Not. R. Astron Soc.* **438** (2014) 1805.
- [8] I. Odderskov, S. Hannestad and J. Brandbyge, *The variance of the locally measured Hubble parameter explained with different estimators*, *J. Cosmol. Astropart. Phys.* **2017** (2017) 022.
- [9] H.-Y. Wu and D. Huterer, *Sample variance in the local measurements of the Hubble constant*, *Mon. Not. R. Astron Soc.* **471** (2017) 4946.

Name	Λ CDM BICEP18	NEDE: Base+BICEP18	NEDE: Base + BICEP18 + SH_0 ES
Ω_m	0.311 0.31072 ± 0.00546	0.308 0.30818 ± 0.00587	0.301 0.30006 ± 0.00518
$\Omega_m h^2$	0.142 0.142337 ± 0.000861	0.147 $0.14654^{+0.00196}_{-0.00435}$	0.153 0.15355 ± 0.00328
Ω_Λ	0.689 0.68920 ± 0.00546	0.692 0.69174 ± 0.00588	0.699 0.69987 ± 0.00518
z_{re}	7.617 7.904 ± 0.714	7.958 7.906 ± 0.724	7.670 8.079 ± 0.735
σ_8	0.809 0.81066 ± 0.00586	0.825 $0.82123^{+0.00853}_{-0.0121}$	0.836 0.84004 ± 0.00963
$\sigma_8/h^{0.5}$	0.984 0.98535 ± 0.00815	0.993 0.98893 ± 0.00877	0.990 0.99320 ± 0.00879
$\sigma_8 \Omega_m^{0.5}$	0.451 0.45187 ± 0.00559	0.458 0.45587 ± 0.00651	0.459 0.46014 ± 0.00671
$\sigma_8 \Omega_m^{0.25}$	0.604 0.60523 ± 0.00553	0.615 $0.61185^{+0.00691}_{-0.00842}$	0.619 0.62171 ± 0.00770
Age [Gyr]	13.789 13.7864 ± 0.0197	13.543 $13.565^{+0.227}_{-0.0838}$	13.194 13.175 ± 0.138
r_s^d	147.277 147.240 ± 0.228	144.705 $144.95^{+2.36}_{-0.891}$	141.263 141.10 ± 1.52
$\sum \chi^2$	4342.37	4339.68	4341.49

Table 9. Best-fit values, means and 1σ confidence intervals for some derived parameters from the MCMC samples involving BICEP18

Dataset	χ^2
Planck 2018 lowl.TT	$21.0697^{+0.5413}_{-0.5784}$ (20.95)
Planck 2018 lowl.EE	$397.0153^{+1.2501}_{-1.1716}$ (395.92)
Planck 2018 lensing.clik	$10.1767^{+0.6169}_{-0.6600}$ (10.08)
Planck 2018 highl plik.TTTEEE	$2361.91^{+6.3973}_{-6.3781}$ (2341.16)
BAO sdss dr7 mgs	$2.153^{+0.4509}_{-0.4515}$ (2.155)
BAO sixdf 2011 bao	$0.0366^{+0.0365}_{-0.0347}$ (0.018)
BAO sdss dr12 consensus bao	$3.734^{+0.3269}_{-0.3147}$ (3.426)
SN Pantheon	$1034.79^{+0.0528}_{-0.0516}$ (1034.73)
ACTPol Lite DR4 for combining w Planck	$242.20^{+4.0044}_{-4.0039}$ (233.67)
SH_0 ES 2021	$3.814^{+3.0903}_{-3.0405}$ (2.188)
Σ	4076.9 (4044.31)

Table 10. Individual χ^2 posteriors means and deviations with the best-fit in parenthesis, for the likelihoods used in the simulation of subsection 3.1 including ACT and sampling over w_{NEDE} .

Dataset	Λ CDM (Base = Planck+BAO+SN)					
	Base	+ACT	+SPT	+ H_0 ES21	+ACT + H_0 ES21	+SPT + H_0 ES21
Pl.18 lowl.TT	23.13	22.63	22.836	22.48	22.25	22.14
Pl.18 lowl.EE	396.81	396.56	395.695	397.69	397.21	397.48
Pl.18 lensing.clik	8.74	8.73	9.418	9.18	8.62	8.95
Pl.18 highl.TTTEEE	2337.97	2338.87	2340.448	2342.27	2339.76	2342.11
bao.sdss dr7 mgs	1.21	1.44	1.340	2.24	1.87	1.97
bao.sixdf 2011 bao	0.03	0.01	0.018	0.03	0.00	0.01
bao.sdss dr12 Cons.	4.51	3.89	4.163	3.46	3.38	3.39
sn.pantheon	1035.05	1034.92	1034.954	1034.73	1034.77	1034.75
ACTPol lite DR4	–	235.33	–	–	235.79	–
SPT3G Y1.TEEE	–	–	1117.716	–	–	1118.68
SH_0 ES	–	–	–	17.98	21.28	20.24
Total χ^2	3807.45	4042.38	4926.589	3830.06	4064.94	4949.71
Q_{dmap}	–	–	–	4.75σ	4.75σ	4.75σ

Table 11. χ^2 values for the individual likelihoods used in the different MCMC analyses, together with the respective totals and Q_{dmap} .

Dataset	NEDE fixed EOS (Base = Planck+BAO+SN)				
	Base	+ACT	+ H_0 ES21	+ACT + H_0 ES21	+ACT fixed m_ϕ
Pl.18 lowl.TT	21.69	21.88	20.73	20.51	21.03
Pl.18 lowl.EE	396.09	395.71	395.92	396.84	395.87
Pl.18 lensing.clik	9.55	9.30	9.83	10.39	9.94
Pl.18 highl.TTTEEE	2336.68	2338.11	2338.51	2340.95	2337.23
bao.sdss dr7 mgs	1.47	1.41	2.05	2.28	1.91
bao.sixdf 2011 bao	0.01	0.01	0.01	0.03	0.00
bao.sdss dr12 Cons.	3.92	3.99	3.44	3.51	3.41
sn.pantheon	1034.88	1034.92	1034.73	1034.74	1034.75
ACTPol lite DR4	–	235.21	–	238.97	235.11
SH_0 ES	–	–	1.52	0.84	–
Total χ^2	3804.26	4040.56	3806.74	4049.05	4039.26
$\Delta\chi^2$	–3.19	–1.82	–23.32	–15.89	–3.13
Q_{dmap}	–	–	1.57σ	2.9σ	–

Table 12. χ^2 values for the individual likelihoods used in the different MCMC analysis involving ACT and corresponding reference runs, together with the respective totals and Q_{dmap} .

Dataset	NEDE fixed EOS (Base = Planck+BAO+SN)				
	Base	+SPT	+ H_0 ES21	+SPT + H_0 ES21	+SPT fixed m_ϕ
Pl.18 lowl.TT	21.686	21.664	20.727	20.749	21.725
Pl.18 lowl.EE	396.087	396.166	395.918	397.283	396.445
Pl.18 lensing.clik	9.545	9.314	9.834	9.851	9.234
Pl.18 highl.TTTEEE	2336.679	2337.241	2338.514	2337.810	2337.021
bao.sdss dr7 mgs	1.465	1.409	2.045	2.331	1.526
bao.sixdf 2011 bao	0.008	0.012	0.010	0.036	0.005
bao.sdss dr12 Cons.	3.918	4.045	3.441	3.564	3.814
sn.pantheon	1034.876	1034.901	1034.735	1034.745	1034.848
SPT3G Y1.TEEE	–	1118.515	–	1118.718	1118.607
SH_0 ES	–	–	1.517	1.494	–
Total chi2	3804.265	4923.266	3806.741	4926.580	4923.224
$\Delta\chi^2$	–3.19	–3.32	–23.32	–23.13	–3.37
Q_{dmap}	–	–	1.57σ	1.82σ	–

Table 13. χ^2 values for the individual likelihoods used in the different MCMC analysis involving SPT and corresponding reference runs, together with the respective totals and Q_{dmap} .

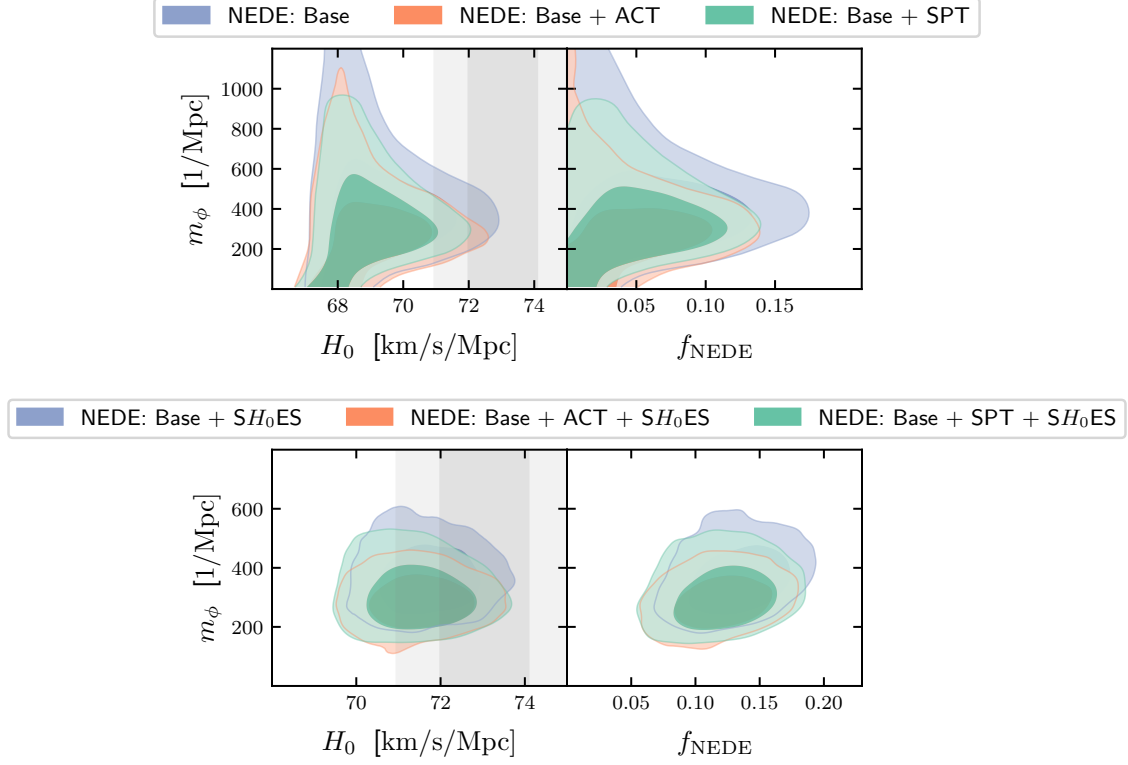


Figure 10. Mass posteriors from the different simulations of NEDE using the baseline datasets. Each plot displays the 68% and 95% C.L. contours for the different dataset combinations. (Upper panels) MCMC runs without SH_0ES . (Lower panels) MCMC runs including the SH_0ES likelihood.

Dataset	LCDM: Base + BICEP18	NEDE: Base + BICEP18	NEDE: Base + BICEP18 + SH_0ES
Planck18 low ℓ TT	23.25	22.16	20.91
Planck18 low ℓ EE	395.99	396.51	395.87
Planck18 high ℓ plik TTTEEE	2338.74	2336.64	2337.51
Planck18 lensing clik	8.84	9.09	9.71
BAO sdss dr7 mgs	1.26	1.41	1.93
BAO sixdf 2011 bao	0.028	0.012	0.004
BAO sdss dr12 consensus	4.37	4.03	3.45
SN Pantheon	1035.01	1034.90	1034.74
BICEP/Keck 2018	534.88	534.93	534.80
SH_0ES21	–	–	2.57
$\sum \chi^2$	4342.37	4339.68	4341.49

Table 14. Individual and total χ^2 values for MCMC runs involving the BICEP18 dataset described in subsection 3.4.

- [10] T.M. Davis, S.R. Hinton, C. Howlett and J. Calcino, *Can redshift errors bias measurements of the Hubble Constant?*, *Mon. Not. R. Astron. Soc.* **490** (2019) 2948.
- [11] E. Di Valentino, O. Mena, S. Pan, L. Visinelli, W. Yang, A. Melchiorri et al., *In the realm of the Hubble tension—a review of solutions*, *Class. Quant. Grav.* **38** (2021) 153001 [2103.01183].
- [12] N. Schöneberg, G. Franco Abellán, A. Pérez Sánchez, S.J. Witte, V. Poulin and J. Lesgourgues, *The H_0 Olympics: A fair ranking of proposed models*, *Phys. Rept.* **984** (2022) 1 [2107.10291].
- [13] J.L. Bernal, L. Verde and A.G. Riess, *The trouble with H_0* , *J. Cosmol. Astropart. Phys.* **10** (2016) 019 [1607.05617].
- [14] K. Aylor, M. Joy, L. Knox, M. Millea, S. Raghunathan and W.L.K. Wu, *Sounds Discordant: Classical Distance Ladder & Λ CDM -based Determinations of the Cosmological Sound Horizon*, *Astrophys. J.* **874** (2019) 4 [1811.00537].
- [15] N. Arendse et al., *Cosmic dissonance: are new physics or systematics behind a short sound horizon?*, *Astron. Astrophys.* **639** (2020) A57 [1909.07986].
- [16] E. Di Valentino et al., *Cosmology intertwined III: $f\sigma_8$ and S_8* , *Astropart. Phys.* **131** (2021) 102604 [2008.11285].
- [17] R.C. Nunes and S. Vagnozzi, *Arbitrating the S_8 discrepancy with growth rate measurements from redshift-space distortions*, *Mon. Not. Roy. Astron. Soc.* **505** (2021) 5427 [2106.01208].
- [18] P. Asadi et al., *Early-Universe Model Building*, 2203.06680.
- [19] S. Joudaki et al., *KiDS-450: Testing extensions to the standard cosmological model*, *Mon. Not. Roy. Astron. Soc.* **471** (2017) 1259 [1610.04606].
- [20] H. Hildebrandt et al., *KiDS-450: Cosmological parameter constraints from tomographic weak gravitational lensing*, *Mon. Not. Roy. Astron. Soc.* **465** (2017) 1454 [1606.05338].
- [21] H. Hildebrandt et al., *KiDS+VIKING-450: Cosmic shear tomography with optical and infrared data*, *Astron. Astrophys.* **633** (2020) A69 [1812.06076].
- [22] KiDS collaboration, *KiDS-1000 Cosmology: Cosmic shear constraints and comparison between two point statistics*, *Astron. Astrophys.* **645** (2021) A104 [2007.15633].
- [23] V. Poulin, T.L. Smith, D. Grin, T. Karwal and M. Kamionkowski, *Cosmological implications of ultralight axionlike fields*, *Phys. Rev. D* **98** (2018) 083525.
- [24] G. D’Amico, L. Senatore, P. Zhang and H. Zheng, *The Hubble Tension in Light of the Full-Shape Analysis of Large-Scale Structure Data*, *J. Cosmol. Astropart. Phys.* **05** (2021) 072 [2006.12420].
- [25] F. Niedermann and M.S. Sloth, *Resolving the Hubble tension with new early dark energy*, *Phys. Rev. D* **102** (2020) 063527.
- [26] F. Niedermann and M.S. Sloth, *New Early Dark Energy is compatible with current LSS data*, *Phys. Rev. D* **103** (2021) 103537 [2009.00006].
- [27] R. Murgia, G.F. Abellán and V. Poulin, *Early dark energy resolution to the Hubble tension in light of weak lensing surveys and lensing anomalies*, *Phys. Rev. D* **103** (2021) 063502 [2009.10733].
- [28] T.L. Smith, V. Poulin, J.L. Bernal, K.K. Boddy, M. Kamionkowski and R. Murgia, *Early dark energy is not excluded by current large-scale structure data*, *Phys. Rev. D* **103** (2021) 123542 [2009.10740].
- [29] T. Simon, P. Zhang, V. Poulin and T.L. Smith, *Updated constraints from the effective field theory analysis of BOSS power spectrum on Early Dark Energy*, 2208.05930.
- [30] F. Niedermann and M.S. Sloth, *New early dark energy*, *Phys. Rev. D* **103** (2021) L041303.
- [31] I.J. Allali, M.P. Hertzberg and F. Rompineve, *Dark sector to restore cosmological concordance*, *Phys. Rev. D* **104** (2021) L081303 [2104.12798].
- [32] K. Freese and M.W. Winkler, *Chain Early Dark Energy: Solving the Hubble Tension and Explaining Today’s Dark Energy*, *Phys. Rev. D* **104** (2021) 083533 [2102.13655].
- [33] F. Niedermann and M.S. Sloth, *Hot new early dark energy*, *Phys. Rev. D* **105** (2022) 063509 [2112.00770].

- [34] F. Niedermann and M.S. Sloth, *Hot New Early Dark Energy: Towards a Unified Dark Sector of Neutrinos, Dark Energy and Dark Matter*, 2112.00759.
- [35] T. Karwal and M. Kamionkowski, *Dark energy at early times, the Hubble parameter, and the string axiverse*, *Phys. Rev. D* **94** (2016) 103523 [1608.01309].
- [36] V. Poulin, T.L. Smith, T. Karwal and M. Kamionkowski, *Early Dark Energy can Resolve the Hubble Tension*, *Phys. Rev. Lett.* **122** (2019) 221301.
- [37] T.L. Smith, V. Poulin and M.A. Amin, *Oscillating scalar fields and the Hubble tension: a resolution with novel signatures*, *Phys. Rev. D* **101** (2020) 063523 [1908.06995].
- [38] V. Poulin, T.L. Smith and A. Bartlett, *Dark energy at early times and ACT data: A larger Hubble constant without late-time priors*, *Phys. Rev. D* **104** (2021) 123550 [2109.06229].
- [39] A. La Posta, T. Louis, X. Garrido and J.C. Hill, *Constraints on prerecombination early dark energy from SPT-3G public data*, *Phys. Rev. D* **105** (2022) 083519 [2112.10754].
- [40] J.C. Hill et al., *The Atacama Cosmology Telescope: Constraints on Pre-Recombination Early Dark Energy*, *Phys. Rev. D* **105** (2022) 123536 [2109.04451].
- [41] T.L. Smith, M. Lucca, V. Poulin, G.F. Abellan, L. Balkenhol, K. Benabed et al., *Hints of early dark energy in Planck, SPT, and ACT data: New physics or systematics?*, *Phys. Rev. D* **106** (2022) 043526 [2202.09379].
- [42] J.-Q. Jiang and Y.-S. Piao, *Toward early dark energy and $n_s=1$ with Planck, ACT, and SPT observations*, *Phys. Rev. D* **105** (2022) 103514.
- [43] G. D'Amico, N. Kaloper and A. Westphal, *General double monodromy inflation*, *Phys. Rev. D* **105** (2022) 103527 [2112.13861].
- [44] K. Enqvist and M.S. Sloth, *Adiabatic CMB perturbations in pre - big bang string cosmology*, *Nucl. Phys. B* **626** (2002) 395 [hep-ph/0109214].
- [45] D.H. Lyth and D. Wands, *Generating the curvature perturbation without an inflaton*, *Phys. Lett. B* **524** (2002) 5 [hep-ph/0110002].
- [46] T. Moroi and T. Takahashi, *Effects of cosmological moduli fields on cosmic microwave background*, *Phys. Lett. B* **522** (2001) 215 [hep-ph/0110096].
- [47] A.A. Starobinsky, *A New Type of Isotropic Cosmological Models Without Singularity*, *Phys. Lett. B* **91** (1980) 99.
- [48] Y. Gouttenoire, G. Servant and P. Simakachorn, *Kination cosmology from scalar fields and gravitational-wave signatures*, 2111.01150.
- [49] M.-X. Lin, G. Benevento, W. Hu and M. Raveri, *Acoustic Dark Energy: Potential Conversion of the Hubble Tension*, *Phys. Rev. D* **100** (2019) 063542 [1905.12618].
- [50] S. Vagnozzi, *Consistency tests of Λ CDM from the early integrated Sachs-Wolfe effect: Implications for early-time new physics and the Hubble tension*, *Phys. Rev. D* **104** (2021) 063524 [2105.10425].
- [51] C.-P. Ma and E. Bertschinger, *Cosmological perturbation theory in the synchronous and conformal Newtonian gauges*, *Astrophys. J.* **455** (1995) 7 [astro-ph/9506072].
- [52] A.D. Linde, *Eternal extended inflation and graceful exit from old inflation without Jordan-Brans-Dicke*, *Phys. Lett. B* **249** (1990) 18.
- [53] F.C. Adams and K. Freese, *Double field inflation*, *Phys. Rev. D* **43** (1991) 353 [hep-ph/0504135].
- [54] E.J. Copeland, A.R. Liddle, D.H. Lyth, E.D. Stewart and D. Wands, *False vacuum inflation with Einstein gravity*, *Phys. Rev. D* **49** (1994) 6410 [astro-ph/9401011].
- [55] D. Blas, J. Lesgourgues and T. Tram, *The Cosmic Linear Anisotropy Solving System (CLASS) II: Approximation schemes*, *J. Cosmol. Astropart. Phys.* **07** (2011) 034 [1104.2933].
- [56] J. Torrado and A. Lewis, *Cobaya: Code for Bayesian analysis of hierarchical physical models*, *J. Cosmol. Astropart. Phys.* **05** (2021) 057 [2005.05290].
- [57] A. Gelman and D.B. Rubin, *Inference from Iterative Simulation Using Multiple Sequences*, *Statist. Sci.* **7** (1992) 457.

- [58] PLANCK collaboration, *Planck 2018 results. V. CMB power spectra and likelihoods*, *Astron. Astrophys.* **641** (2020) A5 [1907.12875].
- [59] F. Beutler, C. Blake, M. Colless, D.H. Jones, L. Staveley-Smith, L. Campbell et al., *The 6dF Galaxy Survey: Baryon acoustic oscillations and the local Hubble constant*, *Mon. Not. R. Astron. Soc.* **416** (2011) 3017.
- [60] A.J. Ross, L. Samushia, C. Howlett, W.J. Percival, A. Burden and M. Manera, *The clustering of the SDSS DR7 main galaxy sample – I. A 4 per cent distance measure at $z = 0.15$* , *Mon. Not. Roy. Astron. Soc.* **449** (2015) 835 [1409.3242].
- [61] BOSS collaboration, *The clustering of galaxies in the completed SDSS-III Baryon Oscillation Spectroscopic Survey: cosmological analysis of the DR12 galaxy sample*, *Mon. Not. Roy. Astron. Soc.* **470** (2017) 2617 [1607.03155].
- [62] PAN-STARRS1 collaboration, *The Complete Light-curve Sample of Spectroscopically Confirmed SNe Ia from Pan-STARRS1 and Cosmological Constraints from the Combined Pantheon Sample*, *Astrophys. J.* **859** (2018) 101 [1710.00845].
- [63] O. Pisanti, A. Cirillo, S. Esposito, F. Iocco, G. Mangano, G. Miele et al., *PARthENoPE: Public Algorithm Evaluating the Nucleosynthesis of Primordial Elements*, *Comput. Phys. Commun.* **178** (2008) 956 [0705.0290].
- [64] ACT collaboration, *The Atacama Cosmology Telescope: a measurement of the Cosmic Microwave Background power spectra at 98 and 150 GHz*, *J. Cosmol. Astropart. Phys.* **12** (2020) 045 [2007.07289].
- [65] ACT collaboration, *The Atacama Cosmology Telescope: DR4 Maps and Cosmological Parameters*, *J. Cosmol. Astropart. Phys.* **12** (2020) 047 [2007.07288].
- [66] SPT-3G collaboration, *Measurements of the E-mode polarization and temperature-E-mode correlation of the CMB from SPT-3G 2018 data*, *Phys. Rev. D* **104** (2021) 022003 [2101.01684].
- [67] BICEP, KECK collaboration, *Improved Constraints on Primordial Gravitational Waves using Planck, WMAP, and BICEP/Keck Observations through the 2018 Observing Season*, *Phys. Rev. Lett.* **127** (2021) 151301 [2110.00483].
- [68] M. Raveri and W. Hu, *Concordance and Discordance in Cosmology*, *Phys. Rev. D* **99** (2019) 043506 [1806.04649].
- [69] PLANCK collaboration, *Planck intermediate results. XVI. Profile likelihoods for cosmological parameters*, *Astron. Astrophys.* **566** (2014) A54 [1311.1657].
- [70] L. Herold, E.G.M. Ferreira and E. Komatsu, *New Constraint on Early Dark Energy from Planck and BOSS Data Using the Profile Likelihood*, *Astrophys. J. Lett.* **929** (2022) L16 [2112.12140].
- [71] A. Reeves, L. Herold, S. Vagnozzi, B.D. Sherwin and E.G.M. Ferreira, *Restoring cosmological concordance with early dark energy and massive neutrinos?*, 2207.01501.
- [72] S. Joudaki et al., *KiDS+VIKING-450 and DES-Y1 combined: Cosmology with cosmic shear*, *Astron. Astrophys.* **638** (2020) L1 [1906.09262].
- [73] DES collaboration, *Dark Energy Survey Year 3 results: cosmological constraints from the analysis of cosmic shear in harmonic space*, *Mon. Not. Roy. Astron. Soc.* **515** (2022) 1942 [2203.07128].
- [74] A.H. Guth, *The Inflationary Universe: A Possible Solution to the Horizon and Flatness Problems*, *Phys. Rev. D* **23** (1981) 347.
- [75] A.D. Linde, *A New Inflationary Universe Scenario: A Possible Solution of the Horizon, Flatness, Homogeneity, Isotropy and Primordial Monopole Problems*, *Phys. Lett. B* **108** (1982) 389.
- [76] PLANCK collaboration, *Planck 2018 results. X. Constraints on inflation*, *Astron. Astrophys.* **641** (2020) A10 [1807.06211].
- [77] F. Lucchin and S. Matarrese, *Power Law Inflation*, *Phys. Rev. D* **32** (1985) 1316.
- [78] A.R. Liddle, *Power Law Inflation With Exponential Potentials*, *Phys. Lett. B* **220** (1989) 502.

- [79] G. D'Amico and N. Kaloper, *Power-law Inflation Satisfies Penrose's Weyl Curvature Hypothesis*, 2208.01048.
- [80] D. Langlois and F. Vernizzi, *Mixed inflaton and curvaton perturbations*, *Phys. Rev. D* **70** (2004) 063522 [astro-ph/0403258].
- [81] F. Ferrer, S. Rasanen and J. Valiviita, *Correlated isocurvature perturbations from mixed inflaton-curvaton decay*, *J. Cosmol. Astropart. Phys.* **10** (2004) 010 [astro-ph/0407300].
- [82] D.A. Easson and B.A. Powell, *Optimizing future experimental probes of inflation*, *Phys. Rev. D* **83** (2011) 043502 [1011.0434].
- [83] W.H. Kinney, A. Moradinezhad Dizgah, B.A. Powell and A. Riotto, *Inflaton or Curvaton? Constraints on Bimodal Primordial Spectra from Mixed Perturbations*, *Phys. Rev. D* **86** (2012) 023527 [1203.0693].
- [84] T. Fujita, M. Kawasaki and S. Yokoyama, *Curvaton in large field inflation*, *J. Cosmol. Astropart. Phys.* **09** (2014) 015 [1404.0951].
- [85] N. Bartolo and A.R. Liddle, *The Simplest curvaton model*, *Phys. Rev. D* **65** (2002) 121301 [astro-ph/0203076].
- [86] N. Bartolo, S. Matarrese and A. Riotto, *On nonGaussianity in the curvaton scenario*, *Phys. Rev. D* **69** (2004) 043503 [hep-ph/0309033].
- [87] M. Boylan-Kolchin, *Stress Testing Λ CDM with High-redshift Galaxy Candidates*, 2208.01611.
- [88] A. Amon et al., *Consistent lensing and clustering in a low- S_8 Universe with BOSS, DES Year 3, HSC Year 1 and KiDS-1000*, 2202.07440.